

SpaRRTa: A Synthetic Benchmark for Evaluating Spatial Intelligence in Visual Foundation Models

Turhan Can Kargin^{1,2*}, Wojciech Jasiński^{1,3}, Adam Pardyl^{1,2,4},
 Bartosz Zieliński¹, Marcin Przewięźlikowski^{1,2}

¹Faculty of Mathematics and Computer Science, Jagiellonian University, Kraków, Poland.

²Doctoral School of Exact and Natural Sciences, Jagiellonian University, Kraków, Poland.

³AGH University of Krakow, Kraków, Poland.

⁴IDEAS NCBR, Warsaw, Poland.

*Corresponding author(s). E-mail(s): turhancan.kargin@doctoral.uj.edu.pl;

Abstract

Visual Foundation Models (VFM)s, such as DINO and CLIP, excel in semantic understanding of images but exhibit limited spatial reasoning capabilities, which limits their applicability to embodied systems. As a result, recent work incorporates some 3D tasks (such as depth estimation) into VFM training. However, VFM performance remains inconsistent across other spatial tasks, raising the question of whether these models truly have spatial awareness or overfit to specific 3D objectives. To address this question, we introduce the Spatial Relation Recognition Task (SpaRRTa) benchmark, which evaluates the ability of VFMs to identify relative positions of objects in the image. Unlike traditional 3D objectives that focus on precise metric prediction (e.g., surface normal estimation), SpaRRTa probes a fundamental capability underpinning more advanced forms of human-like spatial understanding. SpaRRTa generates an arbitrary number of photorealistic images with diverse scenes and fully controllable object arrangements, along with freely accessible spatial annotations. Evaluating a range of state-of-the-art VFMs, we reveal significant disparities between their spatial reasoning abilities. Through our analysis, we provide insights into the mechanisms that support or hinder spatial awareness in modern VFMs. We hope that SpaRRTa will serve as a useful tool for guiding the development of future spatially aware visual models.

Keywords: Visual Foundation Models, 3D awareness, Synthetic data

1 Introduction

Visual Foundation Models (VFM)s such as DINO [1–3] and CLIP [4] demonstrate remarkable performance in semantic visual understanding. Hence, they are widely used for semantic perception tasks including image classification [5], object recognition [6], multimodal learning [7, 8], and scene understanding, with applications in domains such as retail [9] and medical imaging [10]. As

these models move beyond static perception and are increasingly deployed in embodied and interactive settings, their role expands from recognizing visual content to supporting downstream decision-making and interaction [11, 12].

However, effective deployment of VFMs in physical environments requires more than just semantic recognition. To act and navigate, embodied agents must be aware of the spatial properties

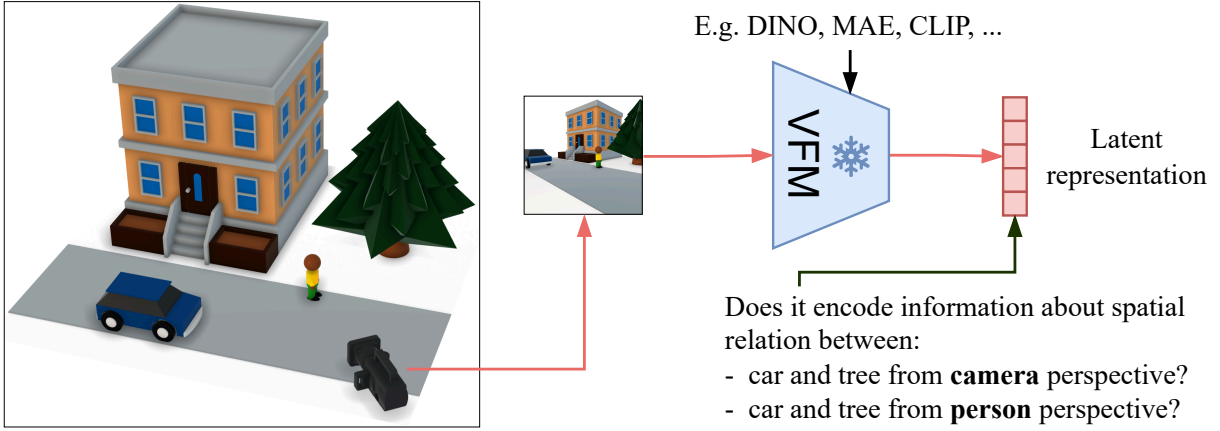


Fig. 1: Effective spatial reasoning requires awareness of spatial relations between visible objects. To analyze such spatial awareness of Visual Foundation Models (VFM), we introduce Spatial Relation Recognition Task (SpaRRTa). We generate images showing different spatial layouts of several objects, encode them with VFM, and probe whether their latent representations reliably encode the information about the spatial relations between the objects from a selected perspective.

of their surroundings, and reason about three-dimensional spatial relations between objects, such as their relative position and perspective (e.g., **the truck is to the left of the tree from the human’s point of view**) [13, 14]. As a result, recent years have seen an increased interest in evaluating VFM in terms of their performance in tasks that require spatial awareness, such as depth prediction, camera pose estimation, and surface normal estimation [15, 16]. Moreover, recent VFM training objectives increasingly incorporate geometric cues [17–20]. While this has yielded improvements in tasks most related to cues used in pretraining, the overall improvements in 3D perception remain inconsistent [15, 16]. This raises a fundamental question: do contemporary VFM acquire a general notion of spatial awareness, or do they instead overfit to specific, quantifiable geometric objectives without capturing abstractions that underpin human spatial understanding?

To address this question, we introduce Spatial Relation Recognition Task (SpaRRTa), a benchmark designed to evaluate abstract spatial awareness in visual representations. Rather than focusing on precise 3D predictions such as distances or surface normals, SpaRRTa targets relational, human-like spatial concepts, including relative position between objects (see Figure 1).

At a conceptual level, identifying relative object positions is a fundamental capability underlying more advanced forms of spatial reasoning [21–23], providing a basis for detailed use cases like navigation, planning, and object manipulation. In practice, SpaRRTa evaluates the efficacy of decoding spatial relation information of given objects from frozen VFM latent representations. By decoupling relational spatial reasoning from precise geometric predictions, SpaRRTa provides a principled way to assess whether VFM represent transferable spatial structure rather than task-specific geometric shortcuts.

SpaRRTa is built with Unreal Engine 5 [24], enabling the generation of photorealistic scenes with a wide range of object categories, layouts, and background contexts (see Figure 2). This synthetic setup provides full control over object placement and precise annotation of spatial relations, allowing evaluation at a scale and diversity that would be prohibitively expensive to obtain from real-world data. By systematically varying object configurations and viewpoints across diverse environments, SpaRRTa enables a controlled and robust evaluation of spatial relation understanding in realistic visual settings, remaining in-distribution for common VFM trained on natural images.

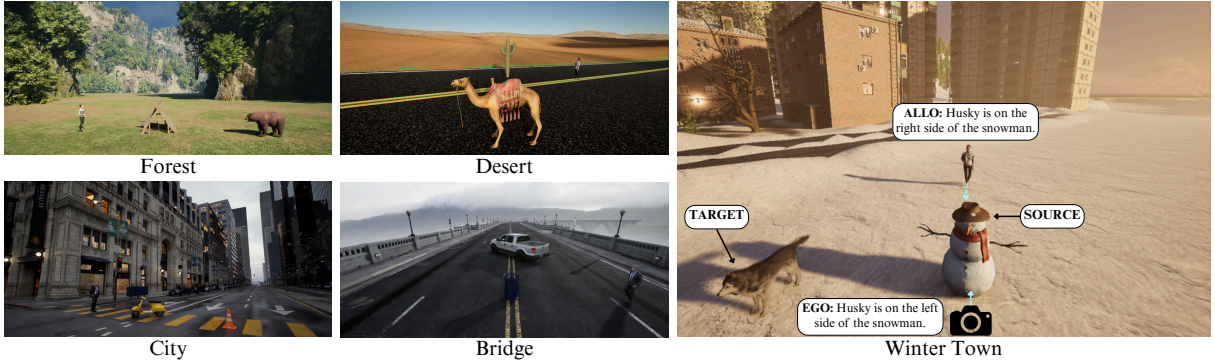


Fig. 2: SpaRRTa evaluates the efficacy of encoding the spatial relations between objects in the image by VFM, either from the camera (**Egocentric**) or an arbitrary object’s (**Allocentric**) perspective (see the right-most image). We use Unreal Engine 5 to produce photorealistic test images that are in-distribution for contemporary VFMs, using a variety of scene environments and object assets.

Using SpaRRTa, we evaluate a broad set of VFMs trained under different supervision regimes and analyze how they encode spatial relations. Our results show that self-supervised VFMs consistently outperform supervised and vision–language models, yet even the strongest models exhibit limitations in perspective-dependent and cluttered settings. By comparing different probing mechanisms, we further reveal that spatial information is primarily stored at the patch level and is largely obscured by global pooling, highlighting the importance of structured aggregation for uncovering spatial knowledge. We hope that SpaRRTa will serve as a useful diagnostic tool for studying spatial representations and for guiding the development of future models with stronger spatial awareness, which is essential for embodied and interactive applications.

Our contributions can be summarized as follows:

- **The Tool:** We introduce SpaRRTa, a photorealistic, synthetically generated evaluation environment built on Unreal Engine 5 for probing spatial reasoning in VFMs.
- **The Benchmark:** We define two standardized challenge sets, SpaRRTa-**ego** (camera-centric) and SpaRRTa-**allo** (allocentric/perspective-taking), designed to disentangle spatial logic from semantic recognition.
- **The Insights:** We benchmark varying families of VFMs (MIM, Joint-Embedding, Supervised, Vision-Language) and characterize which

models provide spatial information in their representations and how these representations are structured.

2 Related Work

Spatial awareness in visual representation learning.

Mainstream self-supervised vision transformers: DINO [1–3], MAE [25], I-JEPA [26] are trained almost exclusively on 2D imagery. They achieve high accuracy on high-level perception tasks, but they can lag behind on depth and multiview geometry when probed or fine-tuned [15, 16]. To bridge this gap, several recent variants inject explicit 3D cues during pre-training: MultiMAE [27], and EmbodiedMAE [28] reconstruct heterogeneous RGB, depth, and semantic segmentation maps; CroCo enforces cross-view completion [17, 18]; SPA [19] trains with differentiable novel-view rendering; Finally, V-JEPA [12] learns to predict future image representations based on conditioned on masked video frames. In contrast to these self-supervised approaches, VGGT [20] adopts a fully supervised paradigm by training a large-scale transformer on a diverse collection of 3D annotation datasets (e.g., Co3D[29], MegaDepth[30]). This approach forces the encoder to internalize a precise geometric structure by directly regressing camera parameters, depth maps, and point tracks. While results still vary across tasks, these methods generally improve depth, pose, and policy-transfer benchmarks [31], suggesting that geometric and

temporal cues are important inductive biases for the next generation of foundation vision encoders. In this work, we introduce a measure of spatial awareness that is more direct than standard metric evaluations (e.g., depth or pose estimation) and conduct a systematic evaluation of the above encoders, providing broader insights about their representations.

Benchmarks for 3D awareness.

3D awareness is usually measured through frozen-encoder probe tasks or task-driven control suites. Probe3D [15] adds decoders for depth, surface normals, and cross-view matching, while the Mid-Level Vision Probe [16] extends this with object segmentation and image similarity. Together, these studies show that higher ImageNet accuracy does not guarantee stronger 3D reasoning and that performance correlates only moderately between probes, highlighting the need for *task-agnostic* diagnostics. Task-driven suites such as VC-1 [31] and SPA [19] utilize the same encoders in navigation and object-search policies, measuring downstream success and thereby tying representation quality to action. Complementing these, several intuitive-physics benchmarks [32–34] test whether a model predicts physically plausible outcomes, an ability adjacent to spatial awareness and vital for embodied agents. Unlike the task-driven or physics-focused evaluations above, our benchmark targets representational 3D knowledge, specifically evaluating abstract, human-like relational spatial reasoning.

Synthetic Environments for Benchmarking.

Synthetic datasets and simulators provide dense, perfectly aligned ground-truth labels that are hard to capture in the wild. For scene-scale perception, RGB-D reconstructions such as ScanNet [35] offer thousands of annotated indoor rooms, though their visual diversity remains limited. Interactive robot benchmarks—Meta-World [36] and Adroit [37] built on MuJoCo [38], and RLBench [39] built on CoppeliaSim [40]—target control dynamics rather than appearance and therefore lack photorealism. At the opposite end of this spectrum, Habitat-Sim [41] renders Matterport3D-style scans [42] at near-photorealistic quality and has

become a widely adopted platform for embodied navigation evaluation. Extending this direction to large-scale outdoor settings, recent works such as FlySearch [43] make use of an environment based on Unreal Engine 5 [24] to evaluate vision language models on the most photorealistic synthetic data to date. In this paper, we explore the use of such environments for evaluating 3D awareness in visual representations.

Probing mechanisms for Vision Transformers

Standard evaluation of Vision Transformer (ViT) based Visual Foundation Models (VFs) typically relies on linear probing (LP) trained on global descriptors, such as the [CLS] token or the Global Average Pooling (GAP) of patch embeddings [25, 44, 45]. This avoids the high computational cost of full fine-tuning and, more importantly, allows to explore the full potential of the pre-trained representations rather than the model’s adaptability. Recent works have introduced selective pooling techniques that recover local information lost by global pooling, such as Attention-Based Multiple Instance Learning Pooling (AbMILP) [45–47], efficient probing [48], or SimPool [49]. The AbMILP method [46] serves as a selective aggregation mechanism, learning a lightweight regressor to assign scalar importance weights to each patch, effectively filtering out background noise and focusing on relevant regions [45]. Unlike simple pooling, efficient probing learns a set of distinct query vectors that attend directly to the input feature space, allowing the probe to generate diverse and complementary attention maps [48, 49]. For instance, attention maps can separately attend to the different objects or different parts of the same object. While the above probing techniques have proved their effectiveness in high-level recognition tasks, we use them to solve fundamental spatial recognition tasks. This allows us to rigorously evaluate the intrinsic spatial awareness of existing VFs and determine whether spatial information is present in their global or local latent space.

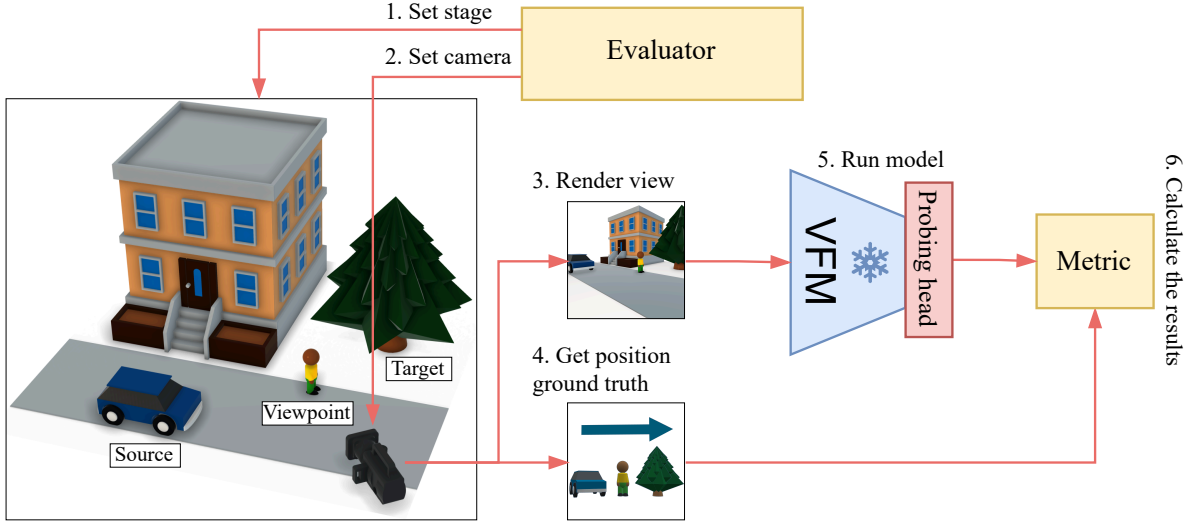


Fig. 3: Evaluation pipeline: The SpaRRTa evaluation setup consists of a data generation system built on Unreal Engine 5. The pipeline begins with an evaluation controller which sets the scene in a precisely controlled manner using a diverse set of realistic assets (1), and places the camera (2) for capture. Next, a near-photorealistic image is rendered by Unreal (3), and ground truth positional information is acquired (4). The image is then passed through evaluated VFM, and resulting representation is fed to the probing head for the positional relation prediction (5). Finally, the accuracy is computed (6).

3 Methodology for Evaluating Spatial Awareness

In this section, we introduce our SpaRRTa methodology for evaluating abstract spatial awareness of visual models. From a high level perspective, SpaRRTa measures the accuracy of recovering the relative spatial configuration of objects placed in a scene based on an image representation. We utilize a two-stage evaluation framework comprising synthetic dataset generation and offline model probing. The entire pipeline, illustrated in Figure 3, and detailed below, follows a structured protocol:

Synthetic Data Generation. The process begins with the experimental design defined by the evaluator.

1. **Set Stage:** The evaluator establishes the scene configuration by selecting a specific environment and assets and randomly positioning the source, target, and viewpoint objects (see Section 3.3 for more details on the used 3D assets.)

2. **Set Camera:** A viewpoint is selected to capture the scene, ensuring that the necessary spatial context is visible from the sensor's perspective. At this stage, the geometric relationship is validated to filter out ambiguous configurations (e.g., where the target lies on a decision boundary), ensuring that only clear cases remain in the dataset (see Section 3.2 for a detailed description of data generation).
3. **Render View:** The Unreal Engine rendering pipeline synthesizes a high-fidelity 2D RGB image of the configured scene.
4. **Get Position Ground Truth:** Based on the exact positions of the objects and a given variant of the task, the image is annotated with the spatial relation to be predicted (see Section 3.1).

Representation Probing. Once the data are generated, we proceed to the evaluation of the visual models.

5. **Run Model:** The images are fed into the VFM. Crucially, the VFM backbone remains

frozen to assess its intrinsic pre-trained representations without further weight adaptation. The extracted features are then passed to a lightweight probing head, which predicts the discrete spatial relation (we detail the benchmarked VFM and probing techniques in Section 4.1).

6. **Calculate Results:** Finally, the model’s predicted spatial relation class is compared to the ground-truth geometric label derived in Step 4 to compute the classification accuracy.

3.1 Spatial Relation Recognition Task

To evaluate spatial awareness of visual models, we define a family of tasks where the objective is to determine the relative spatial relation between objects present in a single image. Given two objects, denoted as **source** and **target**, the task is to classify the direction from the source to the target. We formulate the prediction as a four-way classification problem with discrete labels, i.e. `{left, right, front, back}`. A key aspect of spatial direction is that it is not defined in absolute image coordinates, but with respect to a chosen reference **viewpoint**. In this work, we define a viewpoint as the observer that determines how spatial relations are perceived. We formulate the **egocentric** and **allocentric** variants of the task that differ in the viewpoint used to express the direction. We visualize both variants in Figure 4, and describe them below.

Egocentric variant (Figure 4a) defines the camera as the viewpoint. The question is therefore where the target lies relative to the source as seen from the camera. This variant captures spatial relations directly observable from the input image.

Allocentric variant (Figure 4b) defines the selected third object (in our case, the human) as a viewpoint. In this scenario, the spatial relation observed by the camera differs from the relation observed by the viewpoint object. Consequently, the allocentric variant is more challenging, as it requires the model to decouple the spatial relation from its own visual input. This demands an implicit viewpoint transformation known as perspective-taking. The model must ignore the apparent positions of objects in the image and

infer their geometric arrangement relative to the third object’s perspective.

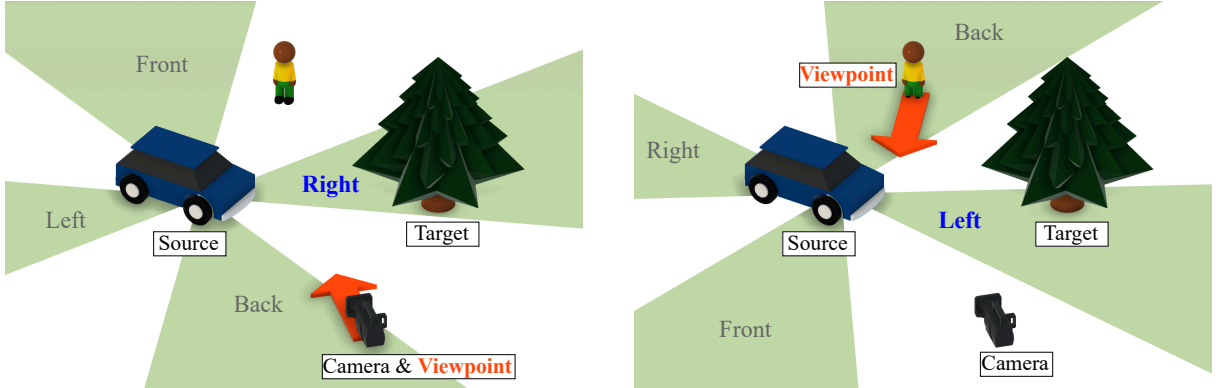
3.2 Data generation pipeline

In contrast to standard vision benchmarks such as ImageNet [5], which rely on images gathered from the Internet, SpaRRTa uses a modern rendering engine to create near-photorealistic images for evaluation. This allows us to retain full control over image content while remaining in-distribution for the common VFM.

Renderer. As rendering engine, we chose Unreal Engine 5 [24] as it provides state-of-the-art rendering quality and performance through real-time ray tracing with dynamic global illumination and reflections, as well as automatically adjusted level of detail. The engine allows for great extensibility and has an open-source codebase, which allows us to extend it for the needs of this study, providing interfaces for both automated environment map creation, image capture, and ground truth acquisition. Moreover, Unreal Engines’ vast online marketplace of free graphical assets, many of which were created using photogrammetry, provides a great source of test evaluation scenario diversity while assuring high-fidelity, realistic results. Finally, it requires relatively modest hardware, such as a consumer-grade GPU, while supporting deep learning dedicated solutions, provided with the Vulkan library.

Scenario generator. The scenario generation part of the pipeline is responsible for procedural generation of diverse testing environments using the official Unreal Engine Editor Python API [50]. First, it randomly selects test objects from a map-specific asset list and places them on the ground at positions sampled from a Gaussian distribution. Next, the camera position is sampled from a uniform distribution over an area surrounding the map center and oriented toward the placed objects. Finally, the system verifies that all assets are correctly loaded and that the scene is ready for image capture. Additional implementation details are provided in Section A.2.

Geometric ambiguity control. A fundamental challenge in spatial classification lies in defining precise boundaries between semantic classes (e.g., determining the exact threshold where *Front* transitions to *Left*). To eliminate label noise and ensure mathematical rigor,



(a) Egocentric Spatial Relation Recognition Task (**SpaRRTa-ego**). In this variant, the camera position defines the viewpoint reference for the spatial directions. The correct relative direction from the **car** (source) to the **tree** (target) is **right**.

(b) Allocentric Spatial Relation Recognition Task (**SpaRRTa-allo**). In this variant, the spatial directions from the reference are defined by a the **viewpoint** object (human). The correct relative direction from the **car** (source) to the **tree** (target) is **left**.

Fig. 4: Visualization of the Spatial Relation Recognition Task (SpaRRTa). The task is to predict the spatial relationship between the **source** (i.e. car) and **target** (tree) objects with respect to a given **viewpoint** (i.e. the camera in the egocentric variant (a), and human in the allocentric variant (b)). To eliminate ambiguity of the tasks, we generate scenes where the spatial relationships of objects are clearly recognizable – the green area denotes valid locations for target placement.

we implement a strict procedural rejection sampling strategy. We define ambiguity zones as $\pm 15^\circ$ angular regions centered along the diagonals ($45^\circ, 135^\circ, 225^\circ, 315^\circ$) relative to the viewpoint’s forward direction. These diagonals serve as the dividing lines between the four main directions. The pipeline computes the precise angular relationship between the target and source objects, and automatically discards any scenario in which the target falls within these ambiguity zones. This guarantees that all retained samples possess indisputable ground-truth labels, ensuring that evaluation metrics reflect genuine spatial reasoning capabilities rather than boundary confusion. We provide a comprehensive description and visualization of these exclusion zones in Section A.1.

Image and ground truth capture. View capture is performed using the adapted UnrealCV library [51]. We capture both the ray-traced RGB image and a ground-truth segmentation mask. The mask is used together with the 3D coordinates of spawned objects to assert the validity of the scenario generation and calculate the ground-truth label for the view (Front, Back, Left, or Right). All captured images and metadata are

stored for model evaluation. Detailed statistics on the dataset size are provided in Section A.1.

3.3 Evaluation Environments

To ensure that SpaRRTa measures robust spatial reasoning rather than overfitting to specific visual domains, we construct a diverse suite of five distinct high-fidelity environments (see Figure 2). These environments range from organic, unstructured landscapes to dense, structured urban settings, challenging the model to generalize geometric understanding across vastly different textures, lighting conditions, and contextual layouts.

Asset Classes. To minimize semantic ambiguity and prioritize spatial reasoning performance, we used a fixed set of distinguishable objects for each environment. Each scene includes a human object who serves as the consistent viewpoint for the allocentric tasks. The source and target objects are selected to be semantically coherent with their respective environments (see Figure 2). This selection ensures that the objects are naturally occurring within the scene context across all evaluation trials. Crucially, our asset selection strategy prioritized objects that are



Fig. 5: SpaRRTa Asset Library. SpaRRTa constructs test examples using a curated set of diverse, high-fidelity 3D assets selected based on common ImageNet classes [5].

not only naturally occurring within their respective scene contexts (e.g., Camels in a Desert, Taxi in a City) but are also statistically prominent in standard pre-training datasets like ImageNet [52]. This way, we ensure that any failure in spatial reasoning is due to geometric understanding rather than a lack of semantic recognition by selecting assets that align with common ImageNet super-categories—(1) *Animals*, (2) *Everyday Objects*, (3) *Nature*, and (4) *Humans*. We provide a catalog of all 3D assets, including their sources in Table 5 and Figure 5.

Environmental diversity. We leverage high-quality environments from the Unreal Engine ecosystem to create photorealistic scenes that mimic real-world complexity. The benchmark consists of the following five distinct types of environment.

- **Forest environment** is based on the Electric Dreams Environment Unreal Engine product demo [53]. This scene depicts a sparse forest landscape with complex foliage, uneven terrain, and natural rock formations.
- **Desert environment** is a vast, arid landscape [54] characterized by open terrain, sand dunes, and high-contrast lighting. This environment is very sparse and texture-homogeneous compared to other environments.

- **Winter Town environment** is a snow-covered setting reflecting a typical small Eastern European town [55]. This environment consists of cold lighting, occluding snow textures, and a small number of village-type buildings.
- **Bridge environment** is a valley scene [56] centered around a large bridge infrastructure.
- **City environment** is a large-scale, modern American metropolis used from the City Sample demo [57], featuring high-rise architecture, paved roads, and complex urban geometry.

3.4 Implementation details

To ensure the reproducibility of our results and the accessibility of the SpaRRTa benchmark to the wider research community, we utilize standard, open-source libraries and consumer-grade hardware for all experiments.

Simulation and Rendering Stack. The synthetic environment generation is built on Unreal Engine 5.5, leveraging its native Python API [50] for scene manipulation and automated asset placement. We employ the UnrealCV plugin [51] to capture synchronized RGB images and segmentation masks. The rendering pipeline runs on a standard Windows workstation equipped with two NVIDIA RTX 2080 Ti (11GB VRAM), generating high-fidelity data without the need for enterprise-grade compute clusters.

Probing and Evaluation Stack. All probing experiments are conducted in a Linux environment using an NVIDIA RTX 4090 (24GB VRAM) graphics card. We follow the established protocols for probing frozen features, specifically the methodology outlined in recent mid-level vision benchmarks [16]. The evaluation framework is implemented in PyTorch, with pre-trained VFM sources directly from the official HuggingFace Transformers or timm libraries to ensure standardized weight initialization. The full codebase, including the Unreal Engine scene generation scripts and probing frameworks, will be made publicly available upon publication.

4 Experiments

In this section, we describe our evaluation of the current prominent Visual Foundation Models (VFM) on the Spatial Relation Recognition Task (SpaRRTa). Section 4.1 details the choice of VFM, as well as the methodology of adapting them for solving SpaRRTa. In Section 4.2, we conduct the evaluation of VFM on SpaRRTa, revealing which models encode spatial relations. In Section 4.3, we compare the efficacy of solving SpaRRTa by VFM with other spatial awareness and high-level image recognition tasks, in order to understand the relationship between these methodologies. Finally, in Section 4.4, we analyze the inner representations of VFM to better understand how spatially-aware representations are formed and where they are expressed.

4.1 Experimental setup

Evaluated Visual Foundation Models (VFM). To systematically evaluate the emergence of spatial reasoning, we curate a diverse suite of VFM spanning distinct learning paradigms, as detailed in Table 1. Our selection prioritizes Self-Supervised Learning (SSL) methods, which we categorize into Joint-Embedding Architectures (JEA) [1–3], and Masked Image Modeling (MIM) [17–19, 25, 59]. Moreover, we compare to several VFM prominent in the community, trained in a supervised and weakly supervised manner [4, 20, 60]. To ensure a fair comparison of learned representations, we evaluate all models using a ViT-Base backbone with an input resolution standardized to 224×224 .

We note two necessary exceptions regarding model size. VGGT [20] provides only ViT-Large checkpoints. We explicitly include VGGT, which is trained with direct 3D supervision (cameras, depth, tracks), to serve as a 3D-native baseline. This allows us to determine if explicit 3D training signals are strictly necessary for the abstract spatial reasoning tasks in SpaRRTa, or if such capabilities can emerge from 2D self-supervision alone. For a fair comparison on the ViT-L backbone, we also add the DINO-v2 (+reg) ViT-Large model [2, 58], a JEA model whose parameters also served as the initialization of the VGGT training [20]. By comparing these two models, we directly analyze the shift in representations of a model pretrained for high-level recognition resulting from adaptation to 3D perception tasks.

Adapting VFM to solving SpaRRTa via probing. At a conceptual level, our approach follows a simple principle: if a pretrained VFM representation contains spatial information, it should be possible to extract it via lightweight probing. By default, we extract the features from the final transformer block (we conduct a detailed analysis of intermediate layers in Section C). Following the protocols established in recent mid-level vision benchmarks [16], we evaluate representations by attaching different types of probing heads to the VFM: (i) linear probing with Global Average Pooling of the patch tokens, as well as Selective Aggregation via (ii) Attention-Based Multiple Instance Learning Pooling (AbMILP) [45, 46], and (iii) Efficient probing [48]. We depict these approaches in Figure 6. Probe (i) evaluates a global representation formed by naively aggregating dense VFM features, while (ii–iii) additionally account for their spatially local nature.

Evaluation protocol. For a given VFM, we evaluate the SpaRRTa performance in terms of the accuracy of probes trained for recognizing the spatial relations of given `source`, `target`, `viewpoint` object triples. Performance on SpaRRTa across images belonging to a given semantic triple therefore reflects the ability to resolve spatial relations for those particular object types, while averaging over diverse semantic triples provides an aggregate measure of spatial relation recognition. For each such triple of objects, we curate a dataset of images depicting different object layouts, and split it into train, validation,

Model	Pre-training Objective	Supervision	Training Dataset
Joint-Embedding (JEA)			
DINO[1]	Contrastive / Distillation	Self-Sup.	ImageNet-1k
DINO-v2 [†] [2]	DINO + iBOT	Self-Sup.	LVD-142M
DINO-v2 (+reg) [‡] [58]	DINO-v2 w/ Register Tokens	Self-Sup.	LVD-142M
DINOv3[3]	DINO + iBOT	Self-Sup.	LVD-1689M
Masked Image Modeling (MIM)			
MAE[25]	Pixel Reconstruction	Self-Sup.	ImageNet-1k
MaskFeat[59]	HOG Feature Prediction	Self-Sup.	ImageNet-1k
SPA[19]	Masked Volumetric Neural Rendering	Multi-View Self-Sup.	ScanNet, Hypersim, S3DIS
CroCo[17]	Cross-View Completion	Self-Sup.	Habitat
CroCov2[18]	Cross-View Completion	Self-Sup.	ARKitScenes, MegaDepth, ...
Supervised & Weakly Supervised			
VGGT*[20]	Multi-Task 3D Regression (Cam, Depth, Tracks)	3D Sup.	Co3D, MegaDepth, etc.
DeiT[60]	Classification + Distillation	Label Sup.	ImageNet-1k
CLIP[4]	Image-Text Contrastive	Text-Image Pairs	Web Image-Text (WIT)

Note: All models utilize a ViT-B/16 backbone unless otherwise marked:

[†]ViT-B/14 [‡]ViT-B/14 & ViT-L/14 *ViT-L/14

Table 1: Evaluated Visual Foundation Models (VFM_s). We consider a range of visual backbones, specifically focusing on Self-supervised methods spanning various forms of supervision (JEA, MIM), as well as prominent supervised models.

Hyperparameter	Linear Probing	AbMILP	Efficient Probing
Optimizer	AdamW		
Weight Decay	0.001		
Scheduler	Cosine Decay		
Learning Rate	$10^{-2}, 10^{-3}, 10^{-4}$		
Dropout	0.2, 0.4, 0.6		
Batch Size	256		
Linear Warmup	200	100	100
Training Epochs	1000	500	500
Method-Specific Architectures			
Hidden Dimension	1 linear layer	2-layer MLP	1 linear layer
Queries (N_q)	–	–	4
Output Dim (D_o)	D_i	D_i	$D_i / 8$

Table 2: Hyperparameters for Spatial Probing. We list the configuration used to train the probing heads (Linear, AbMILP, Efficient Probing) on top of frozen VFM backbones. Training settings are consistent across both egocentric and allocentric tasks.

and test folds in 80/10/10 proportions. We train triple-specific probes for the number of epochs specified in Table 2, using the validation set to select the best-performing probe parameters. We report the test accuracies of probes, and repeat this procedure with 2 random seeds and a diverse selection of 3 distinct object triples per each of the 5 environments (see Section 3.3) to achieve a robust evaluation.

4.2 Spatial Relation Recognition Task results

We evaluate the efficacy of Visual Foundation Models (VFM_s) in solving the Spatial Relation Recognition Task (SpaRRTa) with three probing strategies five environments. We summarize the accuracy on the Egocentric and Allocentric variants of SpaRRTa in Table 3 and Table 4, respectively. Below, we discuss several key findings that characterize how VFM_s encode spatial relations.

Spatial relation information is more accessible in dense patch representations than in global features. Across all evaluated models, we observe a consistent performance hierarchy of **Linear < AbMILP < Efficient Probing** (Figure 7), indicating that spatial aggregation mechanisms capable of selectively emphasizing informative regions are critical for SpaRRTa. Linear probing based on global average pooling assumes that spatial information is uniformly present across patches; in complex scenes, this assumption breaks down, as only patches corresponding to the source, target, or viewpoint

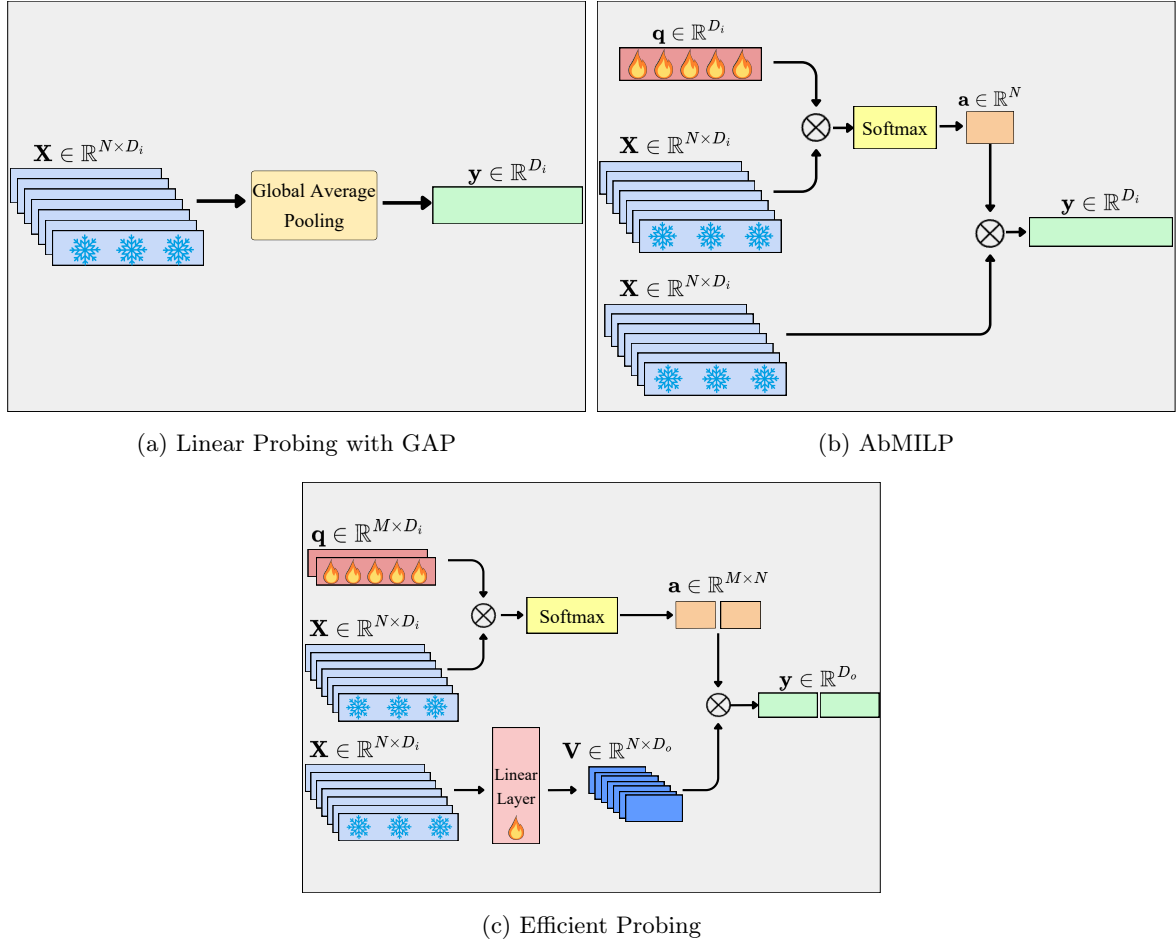


Fig. 6: Architectural comparison of probing protocols on VFM. A frozen VFM backbone processes the input image. Then we apply three different transformations to form a global representation of the image, on top of which we train a linear probe for spatial relation prediction: **Linear Probing with Global Average Pooling (GAP)** aggregates all tokens into a single vector regardless of their relevance (a); **AbMILP** learns a scalar attention map to selectively weight patches (b); **Efficient Probing** utilizes multi query cross attention mechanism with a set of learnable queries (c).

objects are informative, while background patches dilute the signal. AbMILP partially alleviates this issue by learning patch-wise importance weights, leading to consistent improvements over linear probing, particularly in cluttered environments.

This trend is further amplified by the distinction between single-map and multi-query aggregation. While AbMILP compresses selected regions into a single weighted representation via one attention map [45], efficient probing employs multiple learnable queries that can specialize to different spatial entities or scene components [48]. We provide qualitative visualizations of these learned

attention patterns in Section B. For relation-based tasks that require reasoning about multiple distinct objects, this additional capacity provides a consistent advantage.

3D supervision primarily enhances patch-level spatial structure rather than global representations. Different probing mechanisms reveal a counterintuitive divergence when comparing VGGT [20] with its parent model, DINO-v2 (+reg) [2, 58], from which it is initialized and further trained with explicit 3D-awareness supervision. Under linear probing, VGGT does not outperform DINO-v2 and

Model	FOREST			DESERT			Winter Town		
	Lin.	ABM.	Eff.	Lin.	ABM.	Eff.	Lin.	ABM.	Eff.
DINO	64.76	85.53	89.28	55.14	89.34	92.10	61.97	87.05	89.32
DINO-v2 (B/14)	59.91	86.36	91.91	64.57	90.64	93.94	58.03	88.41	93.26
DINO-v2 reg (B/14)	60.81	83.81	91.60	<u>69.40</u>	86.73	94.63	65.38	86.59	91.52
DINO-v2 reg (L/14)	65.37	<u>86.59</u>	93.92	79.68	89.03	96.70	69.02	85.15	<u>94.92</u>
DINOv3	62.41	84.71	<u>93.93</u>	65.34	86.96	<u>97.47</u>	<u>66.14</u>	83.56	93.18
VGGT (L/14)	52.10	89.90	96.18	63.42	<u>90.03</u>	98.78	59.24	<u>87.24</u>	95.53
SPA	52.91	73.01	78.33	49.39	72.58	90.80	49.62	74.01	90.89
CroCo	46.25	75.19	88.98	48.77	80.75	89.88	49.32	83.17	87.95
CroCo v2	54.14	76.18	90.48	52.53	81.91	90.88	53.56	85.20	89.62
CLIP	36.66	55.85	56.33	37.65	56.29	68.44	44.09	61.57	63.21
DeiT	53.23	61.33	75.49	54.75	52.45	78.22	54.24	62.42	75.98
MAE	62.82	84.26	93.10	58.36	87.34	93.71	62.80	85.84	93.26
MaskFeat	47.20	74.60	89.66	<u>42.87</u>	81.52	92.87	<u>47.80</u>	78.63	91.21

Model	Bridge			City			Mean Rank		
	Lin.	ABM.	Eff.	Lin.	ABM.	Eff.	Lin.	ABM.	Eff.
DINO	63.34	89.48	89.86	53.01	83.89	82.45	4.80	3.00	9.20
DINO-v2 (B/14)	66.69	89.63	93.75	53.24	85.31	93.00	5.00	1.40	4.60
DINO-v2 reg (B/14)	67.15	88.49	93.52	<u>57.15</u>	82.98	93.00	3.00	5.20	5.00
DINO-v2 reg (L/14)	69.59	89.40	<u>96.11</u>	64.79	82.38	<u>94.27</u>	1.00	4.20	2.40
DINOv3	<u>67.29</u>	87.11	94.82	56.93	81.63	92.40	<u>2.80</u>	6.40	3.40
VGGT (L/14)	58.92	88.49	96.11	46.08	<u>83.99</u>	94.47	7.00	<u>2.40</u>	1.00
SPA	56.90	<u>77.06</u>	88.72	45.48	69.75	80.27	9.00	11.00	10.00
CroCo	55.57	81.86	92.68	44.88	74.93	87.95	10.80	9.40	9.20
CroCo v2	56.25	83.52	91.01	43.90	<u>77.93</u>	85.99	9.00	7.60	8.40
CLIP	45.35	61.13	64.71	42.92	62.58	<u>64.67</u>	13.00	12.60	13.00
DeiT	56.17	64.10	81.40	43.38	55.50	76.50	9.20	12.40	12.00
MAE	62.50	88.11	93.83	52.87	78.77	89.00	5.00	5.80	4.60
MaskFeat	53.89	82.85	92.30	44.80	72.67	<u>77.64</u>	11.40	9.60	8.20

Table 3: Results on the Egocentric (Camera-Perspective) Task. We report Accuracy (%) across five environments. While most models achieve reasonable performance with Linear probing, efficient probing yields substantial gains, particularly for MIMs (e.g., MAE), which retain rich spatial information in patch tokens that is otherwise lost in global average pooling. Crucially, VGGT achieves state-of-the-art performance across all environments when using efficient probing, demonstrating that explicit 3D supervision yields the richest spatial structure in patch-level representations. **Bold** indicates best, underlined indicates second best. Abbreviations: Lin. (Linear Probing), ABM. (AbMILP), Eff. (Efficient Probing). Each column is colored from the lowest (red color) to the highest value (green color).

in some cases performs slightly worse, indicating that 3D supervision does not substantially improve global image-level representations for spatial relation recognition. In contrast, under AbMILP and efficient probing, VGGT surpasses DINO-v2 on the SpaRRTa task (see Figure 7). This divergence suggests that 3D supervision enriches patch-level geometric structure, which remains largely inaccessible to global pooling

but can be effectively exploited by spatially structured probing mechanisms.

Allocentric spatial relation recognition is consistently more challenging than egocentric recognition. Across all evaluated models, probing strategies, and environments, accuracy on the allocentric variant is systematically lower than on the egocentric variant (see Figure 8). Egocentric relations can be resolved directly from the camera viewpoint, and

Model	FOREST			DESERT			Winter Town		
	Lin.	ABM.	Eff.	Lin.	ABM.	Eff.	Lin.	ABM.	Eff.
DINO	59.09	70.49	69.45	39.78	56.69	57.12	49.21	63.98	64.73
DINO-v2 (B/14)	57.44	73.69	74.42	41.93	64.42	63.80	45.59	66.11	70.26
DINO-v2 reg (B/14)	56.45	70.98	73.11	41.77	60.52	63.14	48.12	65.19	66.92
DINO-v2 reg (L/14)	59.55	73.94	76.66	48.51	61.70	70.30	49.58	68.26	76.35
DINOv3	55.20	67.75	75.31	43.22	59.99	67.45	49.08	61.63	72.38
VGGT (L/14)	51.85	74.81	76.91	39.43	60.85	77.74	42.10	65.91	79.27
SPA	44.57	64.46	70.89	32.55	51.82	63.90	38.59	55.58	66.89
CroCo	44.46	64.95	73.67	32.06	53.52	60.97	37.59	62.59	68.91
CroCo v2	44.17	65.33	73.74	34.35	58.58	60.64	37.81	62.69	68.53
CLIP	40.87	56.97	58.79	29.93	48.56	50.72	36.21	49.37	51.29
DeiT	53.44	58.48	64.38	39.81	40.39	48.18	43.65	47.83	55.21
MAE	51.23	71.06	76.45	35.57	60.88	64.55	41.70	64.92	72.81
MaskFeat	44.28	67.68	73.83	32.11	58.69	61.05	36.14	59.17	69.59

Model	Bridge			City			Mean Rank		
	Lin.	ABM.	Eff.	Lin.	ABM.	Eff.	Lin.	ABM.	Eff.
DINO	48.98	60.61	62.25	48.29	57.78	64.89	3.20	7.60	10.60
DINO-v2 (B/14)	48.38	64.96	69.58	47.08	66.00	70.53	4.20	1.80	4.60
DINO-v2 reg (B/14)	48.61	64.42	65.76	47.75	63.00	66.37	4.00	4.40	8.20
DINO-v2 reg (L/14)	51.05	64.63	77.60	49.70	65.78	73.61	1.20	2.00	1.80
DINOv3	50.04	59.01	69.28	50.21	57.98	68.83	2.60	7.80	4.20
VGGT (L/14)	46.64	65.02	78.15	41.49	62.66	71.19	7.00	3.00	1.20
SPA	40.12	56.99	63.81	37.99	52.95	59.15	10.00	10.80	9.40
CroCo	37.31	62.35	67.35	38.44	60.55	66.01	11.20	8.40	7.80
CroCo v2	37.69	63.08	67.15	38.67	64.75	67.37	10.40	6.40	7.80
CLIP	37.75	51.65	53.29	40.11	50.28	52.73	11.40	12.40	12.80
DeiT	46.86	47.61	56.47	45.35	50.46	60.19	5.80	12.60	12.00
MAE	43.97	62.59	70.61	40.59	62.80	68.88	8.00	4.60	3.40
MaskFeat	35.59	58.27	67.58	38.03	52.47	64.61	12.00	9.20	7.20

Table 4: Results on the Allocentric (Human-Perspective) Task. This task requires implicit perspective taking, causing a significant performance drop compared to the egocentric task. Linear probing fails for most models, hovering near the random baseline. However, VGGT combined with efficient probing achieves the best performance, demonstrating that 3D-supervised features retain precise geometric structure in patch tokens, which patch-aware probes can successfully extract. **Bold** indicates best, underlined indicates second best. Abbreviations: Lin. (Linear Probing), ABM. (AbMILP), Eff. (Efficient Probing). Each column is colored from the lowest (red color) to the highest value (green color).

performance for the strongest models approaches saturation. In contrast, allocentric recognition requires reasoning about spatial relations from a viewpoint that does not coincide with the rendered image, introducing a substantial and persistent performance gap that remains challenging for all tested VFM.

Visual foundation models exhibit a largely consistent hierarchy of spatial recognition performance. Across task variants

and probing strategies, we observe a stable ranking of models in terms of SpaRRTa accuracy (see mean ranks in Table 3 and Table 4). In particular, CLIP [4] and DeiT [60] consistently achieve low performance, indicating that their representations provide limited support for decoding spatial relations. In contrast, the DINO family of models – especially DINO-v2 and DINOv3 [2, 3] pretrained on large-scale datasets—achieve strong and consistent performance across settings. VGGT [20]

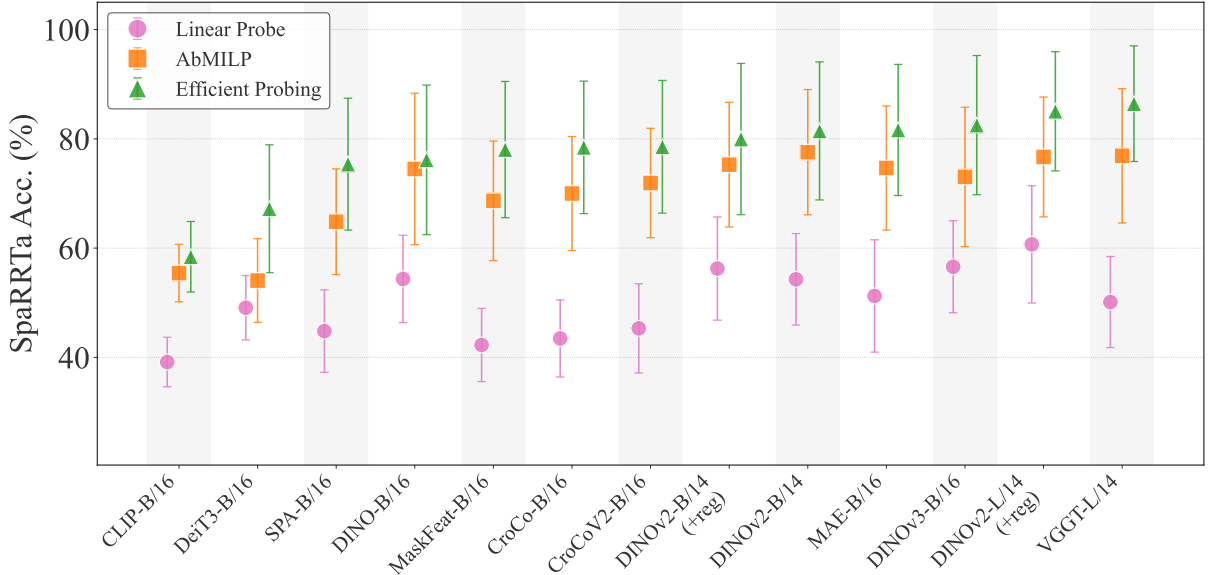


Fig. 7: Impact of Probing Strategy on Spatial Accuracy. We report the aggregated mean accuracy across all five evaluation environments and both tasks (SpaRTA-ego and SpaRTA-allo) for all VFMs. The same performance hierarchy emerges across all backbones (**Linear < AbMILP < Efficient Probing**), indicating that spatial information is primarily encoded in local patch features and largely lost during global pooling.

further improves upon these results under spatially selective probing strategies, reflecting the benefits of explicit 3D supervision. Notably, the Masked Autoencoder (MAE) [25] also achieves competitive performance despite being pretrained on a smaller-scale dataset and using a pixel-level reconstruction objective [61]. Together, these results suggest that spatial relation information is more readily accessible in representations that preserve rich, structured patch-level features.

Environmental complexity significantly affects spatial relation recognition accuracy. As shown in Figure 9, models achieve higher performance in environments with visually homogeneous backgrounds, such as Desert and Forest, and lower performance in scenes with increased semantic clutter, such as City and Winter Town. This performance gap indicates that background complexity and visual noise can interfere with identifying the patches relevant for spatial relation reasoning, making the task more challenging in cluttered environments. The consistency of this trend across models suggests that sensitivity to environmental complexity is a general property

of current visual representations rather than a model-specific artifact.

4.3 Comparison of SpaRTA with other spatial awareness benchmarks

To validate that SpaRTA indeed measures spatial reasoning rather than proxy signals (e.g., low-level texture matching or high-level semantics), we correlate our results with established computer vision benchmarks. We select two mid-level geometric tasks, camera pose estimation and monocular depth estimation [15], and two high-level semantic tasks, FGVC Aircraft [62] and Flowers102 [63] classification. For external benchmarks, we strictly follow standard probing protocols. For classification, we use linear probing on frozen backbones [16]. For depth estimation, we attach a dense prediction transformer (DPT) head [64] as in [15], and for camera pose estimation, we use a 3-layer MLP regressor as in [19]. For SpaRTA, we use the mean accuracy across

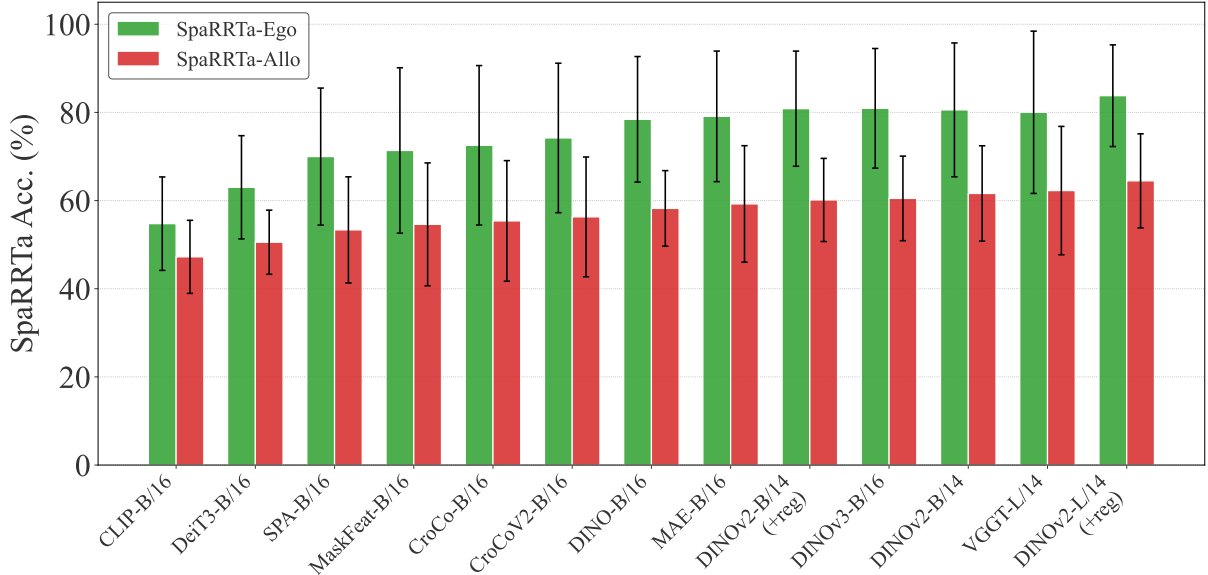


Fig. 8: Impact of Viewpoint Shift on Spatial Accuracy. We report the mean accuracy aggregated across all probing methods and environments for each VFM. The consistent superiority of the egocentric bars (left) over the allocentric bars (right) confirms that resolving spatial relations relative to a non-camera viewpoint is significantly more challenging than reasoning from the camera view, regardless of the underlying model architecture.

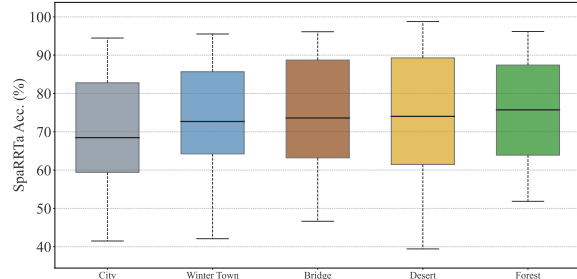
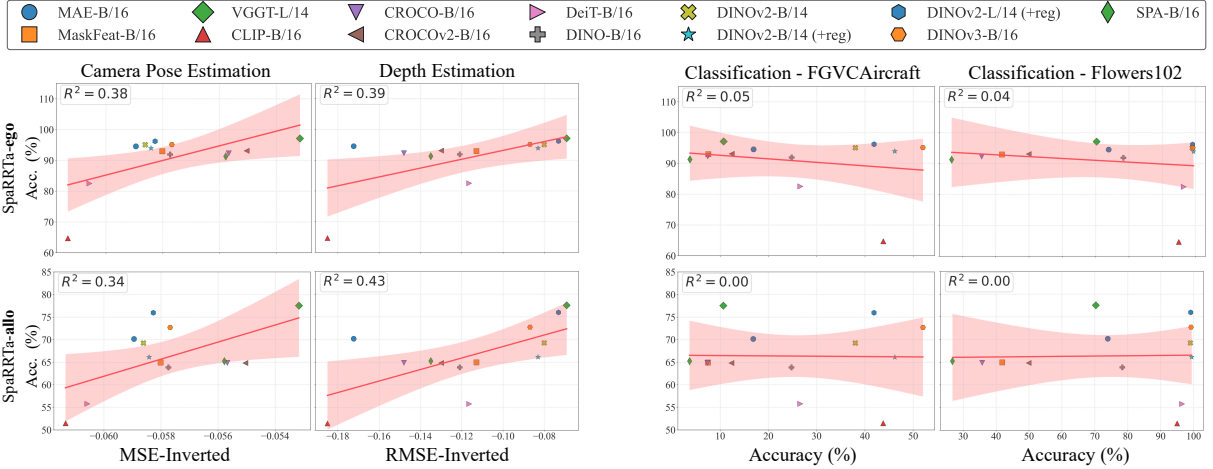


Fig. 9: Influence of Environmental Complexity on Model Performance. We report the accuracy distribution of ViT Large backbones across five evaluation environments, averaged over all probing strategies. Performance peaks in visually homogeneous scenes (e.g., Desert, Forest) but degrades in cluttered scenes (e.g., City). This shows that visual noise makes it harder for models to understand spatial relations.

all five environments obtained by efficient probing [48], as it provides the most robust estimate of a model’s spatial capability.

As evident from Figure 10a, we observe a significant positive correlation between SpaRRTa accuracy and performance on 3D tasks.

Specifically, the allocentric task achieves a coefficient of determination of $R^2 = 0.43$ with depth estimation and $R^2 = 0.34$ with camera pose estimation. This strong relationship confirms that the abstract reasoning required by SpaRRTa is grounded in the same latent geometric representations used for explicit 3D reconstruction. Models with a rich understanding of depth and viewpoint (e.g., VGGT and DINOv3) consistently excel at SpaRRTa, reinforcing the benchmark’s validity as a probe of spatial awareness. We further observe that models pre-trained with explicit multi-view consistency objectives—specifically SPA [19], CroCo [17], and CroCoV2 [18] exhibit higher performance in the camera pose estimation task compared to our tasks and other tasks. We attribute this to their unique pre-training paradigms, which compel the network to internalize camera transformations. CroCo’s cross-view completion objective requires the model to reconstruct masked patches from two different viewpoints of the same scene, effectively learning camera geometry as a latent variable. Similarly, SPA employs volumetric neural rendering to enforce consistency across multiple views from the same scene, directly embedding



(a) Correlation between SpaRTTa performance and 3D mid-level vision tasks.

(b) Correlation between SpaRTTa performance and high-level semantic classification.

Fig. 10: Correlation of SpaRTTa with 3D and Semantic Benchmarks. We compare model accuracy on the SpaRTTa-ego (top) and SpaRTTa-allo (bottom) tasks against four external benchmarks: Camera Pose and Depth Estimation (left) and FGVC Aircraft and Flowers102 Classification (right). We observe a positive correlation ($R^2 \approx 0.40$) with 3D geometric tasks, but a negligible correlation ($R^2 \approx 0.00$) with fine-grained semantic classification. This confirms that SpaRTTa targets latent spatial awareness and is orthogonal to the high-level semantic capabilities, validating SpaRTTa as a distinct and complementary benchmark for VFM evaluation. Note: X-axis metrics (MSE/RMSE) on 3D tasks are inverted so that higher values indicate better performance.

3D spatial structure into the 2D representation. Consequently, these models exhibit a more substantial inductive bias for geometric tasks, which explains their distinct advantage in regressing camera poses.

In contrast, Figure 10b reveals the lack of correlation ($R^2 \approx 0.00$) between SpaRTTa and fine-grained classification benchmarks. High performance in semantic tasks (e.g., identifying flower species) does not predict success in objects' spatial relationships. This result implies that SpaRTTa targets a specific spatial skill set that does not emerge from strong semantic features.

The complete correlation matrix (Figure 11) summarizes these findings. We observe a clear block structure in which spatial tasks (Ego, Allo, Pose, Depth) cluster together, distinct from the semantic classification block. This shows that existing semantic benchmarks are insufficient proxies for the spatial intelligence required by embodied agents. To build truly general vision systems, we must treat 3D awareness as a fundamental, distinct capability axis.

4.4 Analysis of the mechanism of forming spatial representations

In this section, we analyze the mechanism of forming spatial representations in two VFM that tend to achieve the best SpaRTTa performance – DINO-v2 (with register tokens) [2, 58], and VGGT [20]. Apart from their potent spatial representations, the second reason we focus on these models is that the weights of DINO-v2 serve as an initialization for VGGT, which is subsequently trained with a 3D structure perception objective. Therefore, the analysis of these models allows us to characterize not only which properties of representations inform spatial relation encoding, but also the differences between the initial model pre-trained for semantic tasks, and its version tuned for 3D perception.

To investigate why VGGT outperforms DINO-v2 on spatial tasks when using Efficient Probing, yet underperforms with Linear Probing, we analyze the internal attention mechanisms of both backbones. We hypothesize that VGGT's

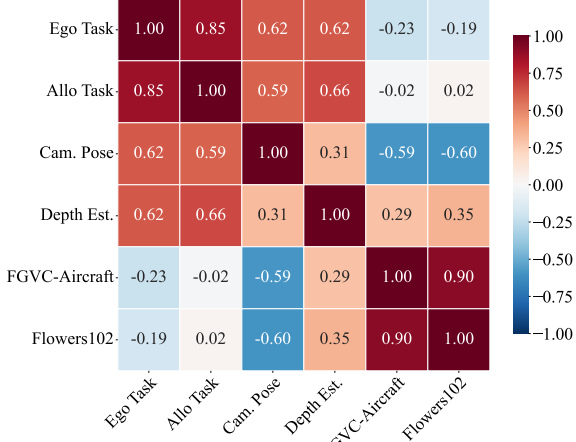


Fig. 11: Pearson Correlation Matrix Across Vision Benchmarks. We visualize the pairwise correlation (r) between our proposed tasks (Ego, Allo) and external benchmarks. A distinct cluster emerges between SpaRRTa and the 3D geometry tasks (Camera Pose, Depth Estimation), while correlations with semantic classification remain weak or negative. This structural separation underscores the importance of evaluating 3D awareness as an independent capability from semantic understanding.

3D supervision forces the model to restructure how information flows between patches, shifting from object-centric feature extraction to relational scene encoding.

Methodology. We conduct this analysis across the five evaluation environments and three objects (Tree, Truck, and Human), selecting 60 clear, non-occluded images per environment where the objects are strictly visible. Using ground-truth segmentation masks obtained from the UnrealCV API [51], we map every patch token to its corresponding object (Human, Tree, Truck, or Background). We then compute the mean attention weights from the source object’s patches to all other regions across all heads in the frozen transformer blocks (see Figure 12). We visualize the layer-wise evolution of these attention scores (averaged across heads and environments) on a logarithmic scale to account for the abundance of background patches.

Model’s attention behavior. We observe that finetuning of VGGT for 3D tasks induces a fundamental reorganization of information flow in

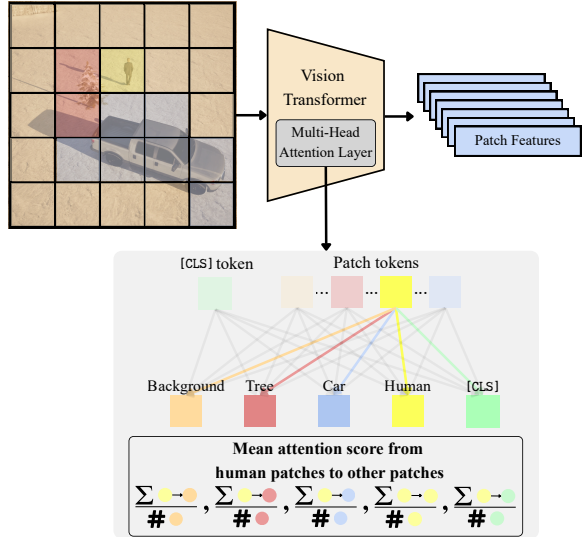


Fig. 12: Methodology for Attention Dynamics Analysis. We illustrate the protocol for mapping patch tokens to semantic categories and calculating the inter-object attention scores. A sample input image is patchified and passed through the frozen ViT backbone to extract raw attention scores between tokens (top). We use ground-truth segmentation masks to assign semantic categories (Background, Tree, Car, Human) to these tokens. Finally, we aggregate patch tokens to compute the mean attention flow between objects (e.g., Human → Car, or Human → [CLS] token) using the formula displayed (bottom).

the deep layers (specifically layers 15–24). As visualized in the VGGT attentions (Figure 14, Bottom Left), we observe a distinct relational shift. The attention from an object to itself (e.g., Human → Human) drops sharper in the final layers of VGGT compared to DINO-v2. At the same time, attention directed toward other objects (e.g., Human → Tree, Human → Truck) exhibits a sharper increase. This redistribution of attention is quantified in the difference plots (VGGT – DINO-v2) presented in Figure 14 (Bottom Right). A clear structural divergence emerges. The differential for the object’s attention itself becomes negative, while the differential for cross-object attention becomes positive. This indicates that VGGT actively repurposes the probability mass previously allocated to local self-refinement and redirects it to encode spatial dependencies between

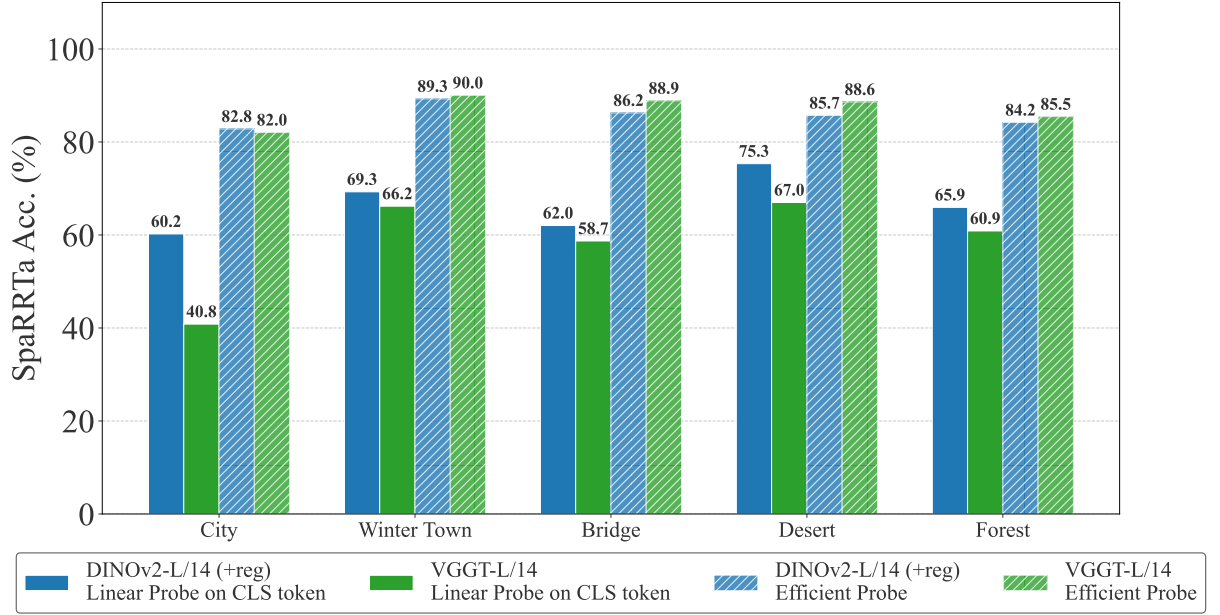


Fig. 13: Linear probing on [CLS] token vs. efficient probing. We compare the spatial reasoning accuracy of DINO-v2 versus VGGT using two probing strategies. We report the mean accuracy averaged across both SpaRRTa-ego and SpaRRTa-*allo* task. DINOv2 outperforms VGGT when linear probing on the global [CLS] token, but VGGT surpasses it with the efficient probe.

distinct entities. Further visualizations and analysis of the attention mechanism for the remaining object classes can be found in Section B.

Implications for Probing Performance.

This structural reorganization provides an explanation for the probing results reported in Section 4.2. To validate this directly, we conducted an experiment comparing linear probing specifically on the [CLS] token versus efficient probing for VGGT and DINO-v2 (see Figure 13). DINO-v2 outperforms VGGT when restricted to the global [CLS] token, yet VGGT surpasses when using the efficient probe. Why does the [CLS] token fail for VGGT? Our analysis in Figure 14 (Top Row) offers the answer. In DINO-v2, the [CLS] token maintains high attention to the objects (e.g., the Truck). This allows the single global vector to retain enough scene context for a linear probe to succeed. In contrast, VGGT’s [CLS] token shifts its attention budget toward register tokens. This suggests that during 3D fine-tuning, VGGT offloads global geometric parameters to registers and distributes object-relative spatial details across the local patch tokens. Consequently, a linear probe on the single [CLS] token fails to access this distributed

information, whereas efficient probing, which aggregates across the entire patch sequence via attention, successfully retrieves the rich spatial context, allowing VGGT to ultimately surpass DINO-v2 in SpaRRTa.

5 Conclusion

Visual Foundation Models (VFM) are a crucial component of embodied applications, encoding optical information about an agent’s surroundings. However, good semantic recognition alone is insufficient for selecting appropriate actions in physical space. In this paper, we introduced Spatial Relation Recognition Task (SpaRRTa), a benchmark for evaluating whether a VFM represents spatial relations between objects in images.

Our results show that while modern VFM contain non-trivial spatial information, this information is not uniformly accessible: spatial relations are primarily encoded at the patch level and are easily obscured by global pooling. As a consequence, standard linear evaluation substantially underestimates spatial awareness, particularly in settings that require perspective-dependent reasoning. We further show that decoding relative

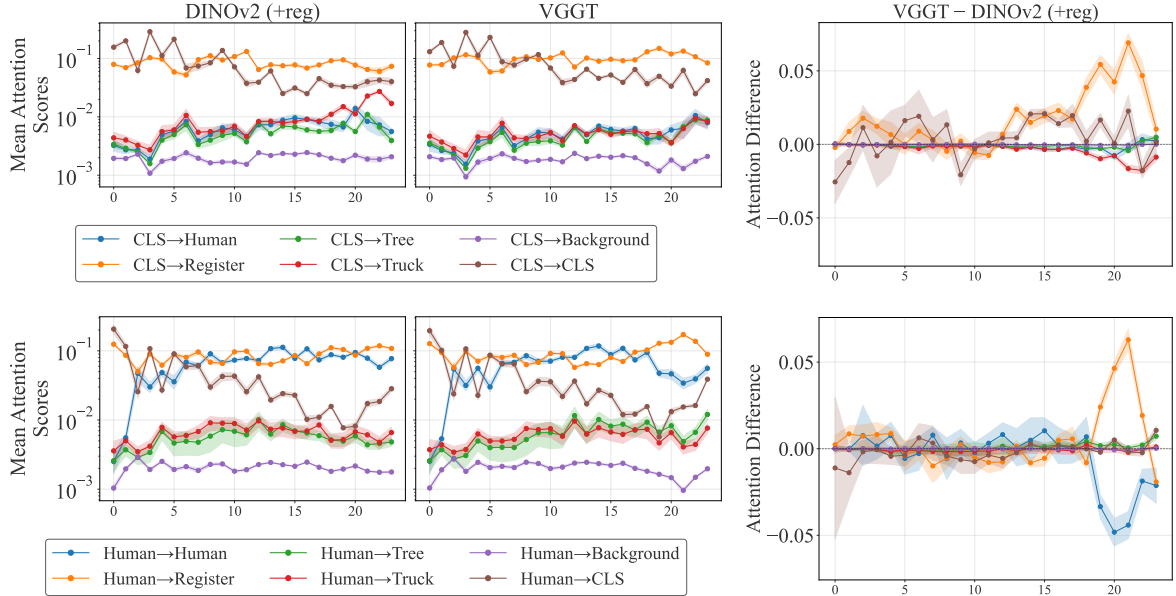


Fig. 14: Comparative Analysis of Attention Flow (DINO-v2 vs. VGGT). We visualize the layer-wise mean attention scores averaged across heads and environments from the global [CLS] token (top row) and human patches (bottom row) to the rest of the patches (Human, Truck, Tree, Background, [CLS] and Register) for both DINO-v2 and VGGT backbones. The two columns on the left show absolute attention scores for DINO-v2 and VGGT, while the right column displays the differential (VGGT – DINOv2) to quantify the divergence in attention dynamics. A fundamental reorganization emerges across all token types in the deeper layers. In the bottom row, while DINOv2 prioritizes attention from human patches to itself or to register tokens (blue and orange negative curves in the difference plot), VGGT consistently reallocates attention to other objects (green and red positive curves in the difference plot). This shows that VGGT’s explicit 3D supervision forces the model to actively encode spatial dependencies between distinct entities.

(allocentric) spatial relations remains challenging across model families, and that explicit 3D supervision primarily improves patch-level geometric structure rather than global representations.

By isolating spatial relation recognition from semantic classification and metric estimation, SpaRRTa provides a complementary evaluation axis that is not captured by existing benchmarks. In the future, we plan to explore the fully controllable synthetic data engine used in SpaRRTa for modeling interactions with the environment and training spatially-aware world models. We hope that SpaRRTa will serve as a diagnostic tool for analyzing spatial representations, and as a guide for developing future vision models with stronger spatial awareness, which is essential for robust embodied perception and decision-making.

Data and code availability

The complete SpaRRTa benchmark dataset, including all generated synthetic images and geometric metadata, will be made publicly available upon publication. To facilitate reproducibility and further research, we will also release the full source code for the Unreal Engine data generation pipeline and the model evaluation framework. The source code will be released at <https://github.com/gmum/SpaRRTa>

Acknowledgements

This research has been supported by the flagship project entitled “Artificial Intelligence Computing Center Core Facility” from the Priority Research Area DigiWorld under the Strategic

Programme Excellence Initiative at the Jagiellonian University. The work of Turhan Can Kargin, Adam Pardyl, and Bartosz Zieliński was supported by National Science Centre (Poland) grant number 2023/50/E/ST6/00469. The research of Marcin Przewięźlikowski was supported by the National Science Centre (Poland), grant no. 2023/49/N/ST6/03268. We gratefully acknowledge Polish high-performance computing infrastructure PLGrid (HPC Center: ACK Cyfronet AGH) for providing computer facilities and support within computational grant no. PLG/2025/018312.

References

- [1] Caron, M., Touvron, H., *et al.*: Emerging properties in self-supervised vision transformers. In: Proceedings of the International Conference on Computer Vision (ICCV) (2021)
- [2] Oquab, M., Darzet, T., *et al.*: Dinov2: Learning robust visual features without supervision. ArXiv **abs/2304.07193** (2023)
- [3] Oriane Siméoni, H.V.V., *et al.*: DINOv3 (2025). <https://arxiv.org/abs/2508.10104>
- [4] Radford, A., Kim, J.W., Hallacy, C., *et al.*: Learning Transferable Visual Models From Natural Language Supervision (2021). <https://arxiv.org/abs/2103.00020>
- [5] Deng, J., Dong, W., *et al.*: Imagenet: A large-scale hierarchical image database. In: 2009 IEEE Conference on Computer Vision and Pattern Recognition, pp. 248–255 (2009). Ieee
- [6] Lin, T., Maire, M., *et al.*: Microsoft COCO: common objects in context. CoRR **abs/1405.0312** (2014) [arXiv:1405.0312](https://arxiv.org/abs/1405.0312)
- [7] Bai, S., Chen, K., *et al.*: Qwen2.5-VL technical report. arXiv preprint arXiv:2502.13923 (2025) [arXiv:2502.13923](https://arxiv.org/abs/2502.13923) [cs.CV]
- [8] Li, B., Zhang, Y., *et al.*: LLaVA-onevision: Easy visual task transfer. Transactions on Machine Learning Research (2025)
- [9] Srivastava, S., Wu, K.: HyperVLM: Hyperbolic space guided vision language modeling for hierarchical multi-modal understanding. In: Second Workshop on Visual Concepts (2025). <https://openreview.net/forum?id=kNWsjLgb3I>
- [10] Sroka-Oleksiak, A., Pardyl, A., Rymarczyk, D., *et al.*: AI-Driven Rapid Identification of Bacterial and Fungal Pathogens in Blood Smears of Septic Patients (2025). <https://arxiv.org/abs/2503.14542>
- [11] Venkataraman, S., Rizve, M.N., Carreira, J., Asano, Y.M., Avrithis, Y.: Is imagenet worth 1 video? learning strong image encoders from 1 long unlabelled video. In: The Twelfth International Conference on Learning Representations (2024). <https://openreview.net/forum?id=Yen1lGns2o>
- [12] Bardes, A., Garrido, Q., *et al.*: Revisiting feature prediction for learning visual representations from video. arXiv:2404.08471 (2024)
- [13] Deitke, M., Han, W., Herrasti, A., *et al.*: RoboTHOR: An Open Simulation-to-Real Embodied AI Platform, pp. 3161–3171. IEEE Computer Society, Los Alamitos, CA, USA (2020). <https://doi.org/10.1109/CVPR42600.2020.00323>
- [14] Linsley, D., Zhou, P., *et al.*: The 3d-pc: a benchmark for visual perspective taking in humans and machines. International Conference on Learning Representations (2025)
- [15] Banani, M.E., Raj, A., Maninis, K.-K., *et al.*: Probing the 3D Awareness of Visual Foundation Models. arXiv (2024). <https://arxiv.org/abs/2404.08636> Accessed 2025-05-16
- [16] Chen, X., Marks, M., Cheng, Z.: Probing the Mid-level Vision Capabilities of Self-Supervised Learning (2024). <https://arxiv.org/abs/2411.17474>
- [17] Weinzaepfel, P., Leroy, V., *et al.*: Croco: Self-supervised pre-training for 3d vision tasks by

cross-view completion. In: Advances in Neural Information Processing Systems (2022)

[18] Weinzaepfel, P., Lucas, T., Leroy, V., et al.: CroCo v2: Improved Cross-view Completion Pre-training for Stereo Matching and Optical Flow. arXiv (2022). <https://arxiv.org/abs/2211.10408>

[19] Zhu, H., Yang, H., Wang, Y., et al.: SPA: 3D Spatial-Awareness Enables Effective Embodied Representation. arXiv (2024). <https://arxiv.org/abs/2410.08208> Accessed 2025-05-16

[20] Wang, J., Chen, M., Karaev, N., Vedaldi, A., Rupprecht, C., Novotny, D.: Vggt: Visual geometry grounded transformer. In: Proceedings of the IEEE/CVF Conference on Computer Vision and Pattern Recognition (2025)

[21] Johnson, S.P., Moore, D.S.: Spatial thinking in infancy: Origins and development of mental rotation between 3 and 10 months of age. *Cognitive Research: Principles and Implications* **5**(1) (2020) <https://doi.org/10.1186/s41235-020-00212-x>

[22] Jechura, T.J.: Animal spatial cognition: Comparative , neural & computational approaches. (2006)

[23] Burgess, N., Maguire, E.A., O'Keefe, J.: The human hippocampus and spatial and episodic memory. *Neuron* **35**(4), 625–641 (2002) [https://doi.org/10.1016/S0896-6273\(02\)00830-9](https://doi.org/10.1016/S0896-6273(02)00830-9)

[24] Epic Games: Unreal Engine. <https://www.unrealengine.com>

[25] He, K., Chen, X., et al.: Masked autoencoders are scalable vision learners. In: Proceedings of the IEEE/CVF Conference on Computer Vision and Pattern Recognition (CVPR), pp. 16000–16009 (2022)

[26] Assran, M., Duval, Q., Misra, I., Bojanowski, P., Vincent, P., Rabbat, M., LeCun, Y., Bal-las, N.: Self-supervised learning from images with a joint-embedding predictive architecture. In: Proceedings of the IEEE/CVF Conference on Computer Vision and Pattern Recognition (CVPR), pp. 15619–15629 (2023)

[27] Bachmann, R., Mizrahi, D., Atanov, A., Zamir, A.: MultiMAE: Multi-modal Multi-task Masked Autoencoders. arXiv (2022). <https://arxiv.org/abs/2204.01678> Accessed 2025-05-16

[28] Dong, Z., Ni, F., Yuan, Y., Li, Y., Hao, J.: EmbodiedMAE: A Unified 3D Multi-Modal Representation for Robot Manipulation. arXiv (2025). <https://arxiv.org/abs/2505.10105> Accessed 2025-05-16

[29] Reizenstein, J., Shapovalov, R., et al.: Common objects in 3d: Large-scale learning and evaluation of real-life 3d category reconstruction. In: Proceedings of the IEEE/CVF International Conference on Computer Vision (ICCV), pp. 10901–10911 (2021)

[30] Li, Z., Snavely, N.: Megadepth: Learning single-view depth prediction from internet photos. In: Proceedings of the IEEE Conference on Computer Vision and Pattern Recognition (CVPR) (2018)

[31] Majumdar, A., Yadav, K., Arnaud, S., et al.: Where are we in the search for an Artificial Visual Cortex for Embodied Intelligence? arXiv (2023). <https://arxiv.org/abs/2303.18240> Accessed 2025-05-16

[32] Riochet, R., Castro, M.Y., Bernard, M., Lerer, A., Fergus, R., Izard, V., Dupoux, E.: Intphys: A framework and benchmark for visual intuitive physics reasoning. CoRR **abs/1803.07616** (2018) [1803.07616](https://arxiv.org/abs/1803.07616)

[33] Bear, D., Braun, M., Bittner, J., Mrowca, D., Zhuang, C., Goyal, R., Lotter, W., Lake, B.M., Malik, J.: Physion: Evaluating physical prediction from vision in humans and machines. CoRR **abs/2106.08261** (2021) [2106.08261](https://arxiv.org/abs/2106.08261)

[34] Bordes, F., Garrido, Q., Kao, J.T., Williams, A., Rabbat, M., Dupoux, E.: Intphys 2: Benchmarking intuitive physics understanding in complex synthetic environments.

CoRR **abs/2506.09849** (2025) [2506.09849](https://arxiv.org/abs/2506.09849)

[35] Dai, A., Chang, A.X., Savva, M., *et al.*: ScanNet: Richly-annotated 3d reconstructions of indoor scenes. In: Proc. Computer Vision and Pattern Recognition (CVPR), IEEE (2017)

[36] Yu, T., al.: Meta-world: A benchmark and evaluation for multi-task and meta reinforcement learning. Proc. CoRL (2020)

[37] Rajeswaran, A., Kumar, V., Gupta, A., Todorov, E., Abbeel, P., Levine, S.: Learning complex dexterous manipulation with deep reinforcement learning and demonstrations. In: Robotics: Science and Systems (RSS) (2018)

[38] Todorov, E., Erez, T., Tassa, Y.: Mujoco: A physics engine for model-based control. In: IEEE/RSJ International Conference on Intelligent Robots and Systems (IROS), pp. 5026–5033 (2012). <https://doi.org/10.1109/IROS.2012.6386109> . IEEE

[39] James, S., Davison, A.J.: Rlbench: The robot learning benchmark and learning environment. IEEE Robotics and Automation Letters **5**(2), 3019–3026 (2020)

[40] Rohmer, E., Singh, S.P.N., Freese, M.: Vrep: A versatile and scalable robot simulation framework. In: IEEE/RSJ International Conference on Intelligent Robots and Systems (IROS), pp. 1321–1326 (2013). <https://doi.org/10.1109/IROS.2013.6696520> . IEEE

[41] Manolis Savva, Abhishek Kadian, Oleksandr Maksymets, *et al.*: Habitat: A Platform for Embodied AI Research. In: Proceedings of the IEEE/CVF International Conference on Computer Vision (ICCV) (2019)

[42] Chang, A., Dai, A., Funkhouser, T., Halber, M., Niessner, M., Savva, M., Song, S., Zeng, A., Zhang, Y.: Matterport3d: Learning from rgb-d data in indoor environments. International Conference on 3D Vision (3DV) (2017)

[43] Pardyl, A., Matuszek, D., Przebieracz, M., Cygan, M., Zieliński, B., Wołczyk, M.: Fly-Search: Exploring how vision-language models explore (2025). <https://arxiv.org/abs/2506.02896>

[44] He, K., Fan, H., Wu, Y., Xie, S., Girshick, R.: Momentum contrast for unsupervised visual representation learning. In: Proceedings of the IEEE/CVF Conference on Computer Vision and Pattern Recognition (CVPR) (2020)

[45] Przewięźlikowski, M., Balestriero, R., Jasiński, W., Śmieja, M., Zieliński, B.: Beyond [cls]: Exploring the true potential of Masked Image Modeling representations (2025). <https://arxiv.org/abs/2412.03215>

[46] M., I., *et al.*: Attention-based deep multiple instance learning. In: ICML (2018)

[47] D., R., A., B., J., T., B., Z.: Kernel self-attention for weakly-supervised image classification using deep multiple instance learning. In: WACV (2021)

[48] Bill Psomas, D.C., et al.: Attention, Please! Revisiting Attentive Probing Through the Lens of Efficiency (2025). <https://arxiv.org/abs/2506.10178>

[49] Psomas, B., Kakogeorgiou, I., Karantzalos, K., Avrithis, Y.: Keep it simpool: Who said supervised transformers suffer from attention deficit? In: Proceedings of the IEEE/CVF International Conference on Computer Vision (ICCV), pp. 5350–5360 (2023)

[50] Unreal Python API Documentation. Accessed: 2025-12. https://dev.unrealengine.com/documentation/en-us/unreal-engine/python-api/?application_version=5.5

[51] Qiu, W., Zhong, F., et al.: UnrealCV: Virtual worlds for computer vision. ACM Multimedia Open Source Software Competition (2017)

[52] Ridnik, T., Ben-Baruch, E., Noy, A., Zelnik-Manor, L.: ImageNet-21K Pretraining for the Masses (2021). <https://arxiv.org/abs/2104.10972>

[53] Games, E.: Electric Dreams Environment. <https://www.fab.com/listings/d79688f5-29be-4fb2-a650-2d4a813f5306>. Accessed: 2025-12

[54] Marketplace, U.E.: Desert Landscape. <https://www.fab.com/listings/3d1ccab4-8a4c-470f-a5b8-4a91ca5040d1>. Accessed: 2025-12

[55] Marketplace, U.E.: Winter Town Environment. <https://www.fab.com/listings/5bd7045e-b0ae-45a4-ab00-72b2060ab4c5>. Accessed: 2025-12

[56] Marketplace, U.E.: Bridge Scene. <https://www.fab.com/listings/a472df9d-9179-4743-8d41-335f9ef55546>. Accessed: 2025-12

[57] Games, E.: City Sample. <https://www.fab.com/listings/4898e707-7855-404b-af0e-a505ee690e68>. Accessed: 2025-12

[58] Darcet, T., Oquab, M., Mairal, J., Bojanowski, P.: Vision Transformers Need Registers. arXiv (2023). <https://doi.org/10.48550/ARXIV.2309.16588>. <https://arxiv.org/abs/2309.16588>

[59] Wei, C., et al.: Masked Feature Prediction for Self-Supervised Visual Pre-Training (2023). <https://arxiv.org/abs/2112.09133>

[60] Touvron, H., Cord, M., Jégou, H.: DeiT III: Revenge of the ViT (2022). <https://arxiv.org/abs/2204.07118>

[61] Balestrieri, R., LeCun, Y.: How learning by reconstruction produces uninformative features for perception. In: Proceedings of the 41st International Conference on Machine Learning (2024)

[62] Subhransu Maji, E.R., et al.: Fine-Grained Visual Classification of Aircraft (2013). <https://arxiv.org/abs/1306.5151>

[63] Nilsback, M.-E., Zisserman, A.: Automated flower classification over a large number of classes. In: Indian Conference on Computer Vision, Graphics and Image Processing (2008)

[64] Ranftl, R., Bochkovskiy, A., Koltun, V.: Vision transformers for dense prediction. In: 2021 IEEE/CVF International Conference on Computer Vision (ICCV), pp. 12159–12168 (2021). <https://doi.org/10.1109/ICCV48922.2021.01196>

[65] Fab: Scanned 3D People Pack. <https://www.fab.com/listings/2e872a96-686e-4955-8256-82fa19904f92>. Accessed: 2025-12

[66] Fab: Generic Vehicle Pack. <https://www.fab.com/listings/2909157b-ddfa-4cef-a925-69dc2467021f>. Accessed: 2025-12

[67] Sketchfab: Brown Bear. <https://skfb.ly/oMBYX>. Accessed: 2025-12

[68] Sketchfab: Red Fox. <https://skfb.ly/oRVHD>. Accessed: 2025-12

[69] Sketchfab: Camping Tent. <https://skfb.ly/oLFuS>. Accessed: 2025-12

[70] Fab: Camel 3D Model. <https://www.fab.com/listings/927e49ce-b6ed-4a34-abff-c5b8695626d1>. Accessed: 2025-12

[71] Sketchfab: Barrel. <https://skfb.ly/6SzJ9>. Accessed: 2025-12

[72] Sketchfab: Cactus Model. <https://skfb.ly/oUKJn>. Accessed: 2025-12

[73] Sketchfab: Siberian Husky. <https://sketchfab.com/3d-models/husky-76535348338143219a7ed52772c6c1c2>. Accessed: 2025-12

[74] Sketchfab: Deer. <https://skfb.ly/oHEYJ>. Accessed: 2025-12

[75] Sketchfab: Snowman. <https://sketchfab.com/3d-models/snowman-fbd3d69cd8244aa9c6400ed77cbe1b5>. Accessed: 2025-12

[76] Fab: Bicycle Asset. <https://www.fab.com/listings/de7b5673-a45f-46f0-a4bf-8b3b80421ccd>. Accessed: 2025-12

[77] Sketchfab: Vespa Scooter. <https://skfb.ly/oLnGP>. Accessed: 2025-12

[78] Sketchfab: Traffic Cone. <https://skfb.ly/6SqHs>. Accessed: 2025-12

[79] Sketchfab: Fire Hydrant. <https://skfb.ly/ooUUA>. Accessed: 2025-12

[80] Schneider, P.J., Eberly, D.H.: Chapter 11 - intersection in 3d. In: Geometric Tools for Computer Graphics. The Morgan Kaufmann Series in Computer Graphics, pp. 481–662. Morgan Kaufmann, San Francisco (2003)

[81] Bolya, D., Huang, P.-Y., Sun, P., et al.: Perception Encoder: The best visual embeddings are not at the output of the network. arXiv (2025). <https://arxiv.org/abs/2504.13181>

A Dataset Generation Methodology

A.1 Core Design Principles and Controllability

The design of SpaRRTa is governed by the need to disentangle spatial reasoning from low-level visual pattern matching while ensuring mathematically rigorous ground-truth labels. Unlike real-world datasets, where camera angles and object placements are biased by human photographers, our synthetic approach enables precise control over three critical axes: geometric validity, environmental diversity, and task complexity.

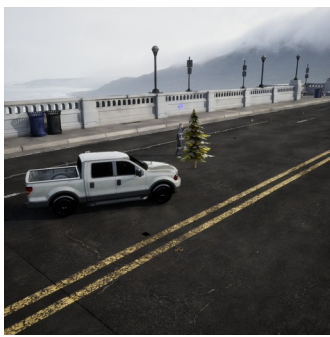
Defining spatial relations and ambiguity. As illustrated in Figure 15, the core challenge of SpaRRTa lies in resolving spatial relations relative to a specific coordinate frame of the viewpoint. Figure 15a shows examples of views from the Unreal Engine environment showing the source object (tree), target object (truck), and human agent. Figure 15b shows the three-dimensional spatial arrangement of the camera

frustum, objects, and human agent in world coordinates. For the egocentric task (Figure 15c, gray arrow), the front direction is defined by the vector from the camera to the source object. For the allocentric task (Figure 15c, red arrow), the front is defined by the vector from the human agent to the source object. A fundamental challenge in spatial classification is defining boundaries between classes (e.g., when does Left become Front?). To ensure the benchmark’s validity, we handle those geometric boundaries. We define ambiguity zones as conical regions (shaded red and gray in Figure 15c) centered around the 45°, 135°, 225°, and 315° diagonals relative to the viewpoint’s forward vector. Any sample in which the target object falls within these zones is automatically filtered from the dataset. This guarantees that the ground-truth labels (left, right, front, back) are unambiguous and robust to minor variations in pose estimation, forcing the model to learn precise spatial boundaries rather than guessing on the margins.

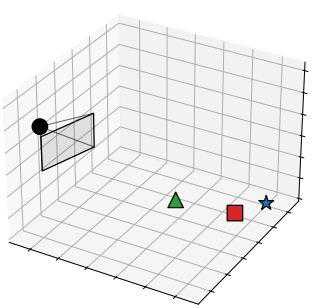
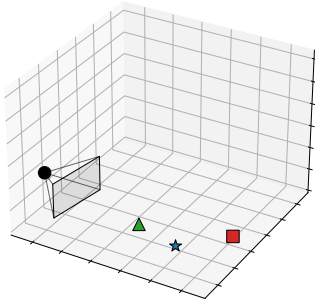
Asset curation and environmental diversity. To test the robustness of spatial representations, we use five distinct environments in SpaRRTa benchmark. We curate specific asset sets for each environment to maintain semantic coherence, ensuring objects appear in natural contexts while preserving geometric consistency. Crucially, we select isotropic objects (rock, tree, traffic cone) as source objects. Their rotationally symmetric nature simplifies the definition of relative positions, ensuring that the spatial relation (e.g., Left of the Tree) is defined purely by the target’s position relative to the source’s center, minimizing ambiguity caused by the source object’s own orientation. The assets we used in our benchmark are detailed in Table 5.

Dataset size and generalization. To determine the optimal data scale, we analyzed model generalization across tasks. We found that **5,000 images** per environment were sufficient for models to generalize on the egocentric task. However, the allocentric task, which requires learning a more complex perspective transformation, exhibited signs of overfitting at this scale. Consequently, we increased the allocentric dataset size to **10,000 images** per environment, ensuring sufficient diversity for the model to learn the underlying geometric rules rather than memorizing specific scene configurations.

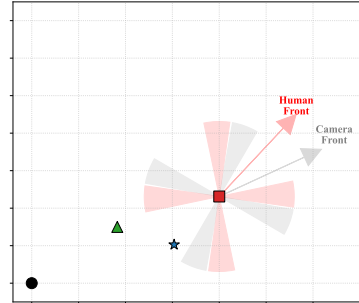
 Source Object
  Target Object
  Camera
  Human



(a) Input RGB image



(b) 3D scene layout



(c) 2D scene logic

Fig. 15: Visualization of Task Geometry and Ambiguity Filtering. We present the geometric construction of SpaRRTa samples, showing the rendered RGB input (a), the global 3D arrangement of assets (b), and the 2D logic for defining the egocentric (gray) and allocentric (red) spatial positions (c).

A.2 Rendering Pipeline Details

Our approach leverages the native Unreal Engine Python API [50] and the UnrealCV plugin [51] to programmatically control object placement, physics validation, and camera logic. The pipeline outputs raw RGB renders, serializes the precise 6-DoF state (position: x, y, z and rotation: ϕ, θ, ψ) of every task-critical objects and camera into JSON metadata files, and generates pixel-perfect instance masks of the source, target, and human objects.

Terrain adaptation via raycasting. We employ a rejection sampling strategy to ensure physical plausibility and visual clarity. We implement a physics-aware placement logic to handle

uneven terrain (e.g., the Forest and Desert environments) without objects floating or clipping. For every object coordinate, the pipeline performs a vertical line trace to detect the exact Z-height of the landscape geometry. Objects are then spawned at the detected ground level, with their specific bounding box offsets applied to ensure flush contact.

Visibility and occlusion control. We enforce visibility constraints at the generation level to guarantee that all task-critical objects are captured. Candidate object positions are validated against the camera's viewing frustum by computing the angular deviation of each object relative to the camera's optical axis. We enforce a strict constraint where the maximum angular

Environment	Asset Class	Source
Global	Humans	Fab [65]
	Vehicle (Car and Taxi)	Fab [66]
	Tree	Environment Pack [53]
Forest	Brown Bear	Sketchfab [67]
	Fox	Sketchfab [68]
	Camping Tent	Sketchfab [69]
	Rocks	Environment Pack [53, 54]
Desert	Camel	Fab [70]
	Barrel	Sketchfab [71]
	Cactus	Sketchfab [72]
	Rocks	Environment Pack [53, 54]
Winter Town	Husky	Sketchfab [73]
	Deer	Sketchfab [74]
	Snowman	Sketchfab [75]
Bridge	Bicycle	Fab [76]
	Trash Can	Environment Pack [56]
City	Motorcycle	Sketchfab [77]
	Traffic Cone	Sketchfab [78]
	Fire Hydrant	Sketchfab [79]

Table 5: SpaRTa Asset Registry. We list the specific 3D assets used across environments. Sources denote the origin of the 3D model.

offset must remain within the camera’s horizontal field of view to prevent objects from being cut off at the frame edges. Furthermore, to ensure appropriate scene composition, we reject configurations where objects appear too clustered or distant, forcing the camera to capture a meaningful spatial spread. Finally, we utilize AABB (Axis-Aligned Bounding Box) [80] overlap checks to prevent inter-object collisions.

Camera configuration and object placement. We standardize the optical setup across all environments to prevent intrinsic camera parameters from becoming a confounding variable. All scenes are rendered using a simulated 50mm lens on a 50mm sensor width, resulting in a consistent horizontal field of view. The camera positioning follows a hierarchical stochastic process. Object coordinates are sampled around a randomly selected center point, with a distance limit to ensure they remain close enough to be distinguishable. The camera is then spawned within a broad area surrounding this group, with its height randomized relative to the average elevation of the objects. Finally, the pipeline computes the geometric centroid of the relevant scene objects (source, target, human agent) and dynamically locks the camera’s rotation to center this cluster, ensuring the primary task elements remain the focal point.

B Extended Attention Visualizations

B.1 Attention Dynamics across Object Categories

In Section 4.4, we identified a relational reorganization of attention in the VGGT backbone. Specifically, we observed that for the global [CLS] token and the Human patches. To verify that this mechanism is a universal property of rather than an artifact specific to the [CLS] token or Human patches, we extend our analysis to other objects. Figure 16 visualizes the layer-wise attention dynamics for the Truck and Tree tokens. Consistent with the findings in Section 4.4, both category of objects exhibit similar structural change. As shown in Figure 16 (Right), VGGT consistently redirects objects’ attention toward other scene entities (positive difference for Truck→Human/Tree, negative difference for Truck→Truck). This confirms that explicit 3D supervision forces the entire spatial representation to shift from object-centric feature extraction to relational scene encoding, regardless of the source token’s semantic category.

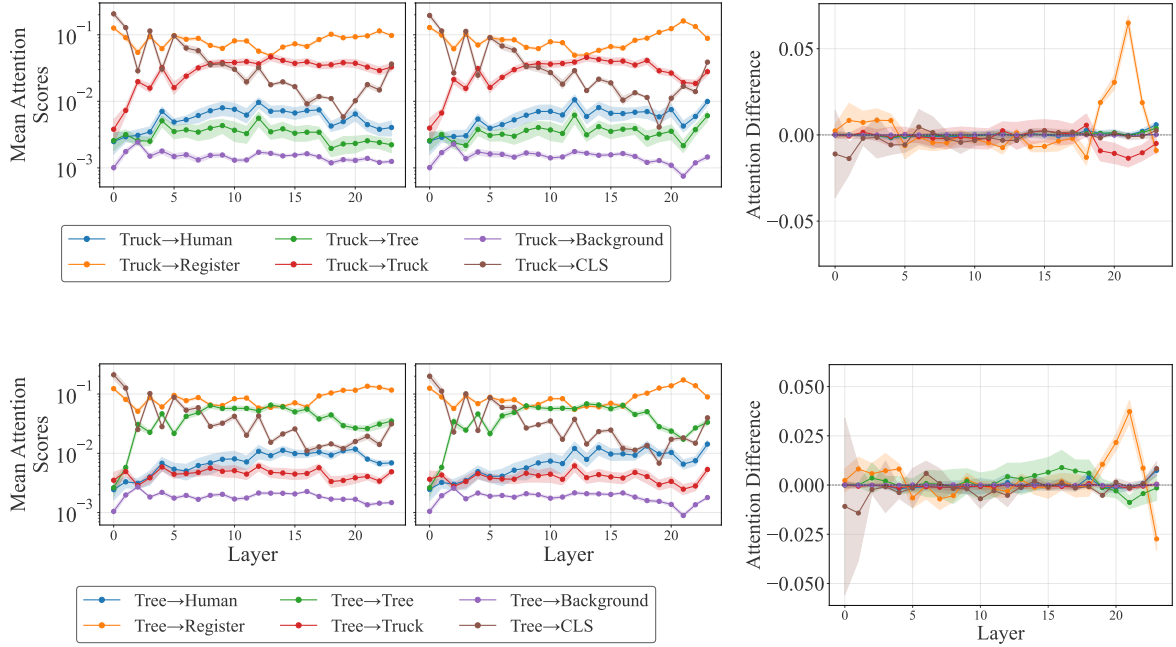


Fig. 16: Further Analysis of Attention Flow (DINO-v2 vs. VGGT). We visualize the layer-wise mean attention scores from Truck (Top) and Tree (Bottom) tokens to the rest of the patches.

B.2 Attention Maps of Efficient Probing

In Figure 17, we visualize the mean attention maps generated by the efficient probing head attached to the frozen VGGT backbone to interpret how the model solves these spatial tasks. These visualizations show that the attention focus changes depending on the task. For the egocentric task (Columns 2 and 5), the model attends to the source and target objects while ignoring the other object. However, when the allocentric task (Columns 3 and 6) is solved, the model attends to the non-camera-viewpoint object, the source, and the target. This dynamic behavior confirms that the probe does not merely memorize texture but actively identifies and disentangles the specific geometric entities, viewpoint, source, and target, required to resolve the spatial query in the correct coordinate frame.

In Figure 18, we visualize the individual attention maps of the four learnable queries ($q_1 \dots q_4$), to understand how efficient probing solves spatial reasoning. This breakdown reveals that rather than collapsing the scene into a single coarse,

global point, the queries diversify to attend to distinct geometric entities. In the egocentric task, we observe that queries tend to split their focus between the source and target objects. Crucially, in the allocentric task, queries often split their attention between the non-camera-viewpoint object and other objects. This behavior confirms that the multi-query architecture forces the model to decompose the scene into its functional components, viewpoint, source, and target, providing the downstream classifier with a structured, part-based representation of the geometry.

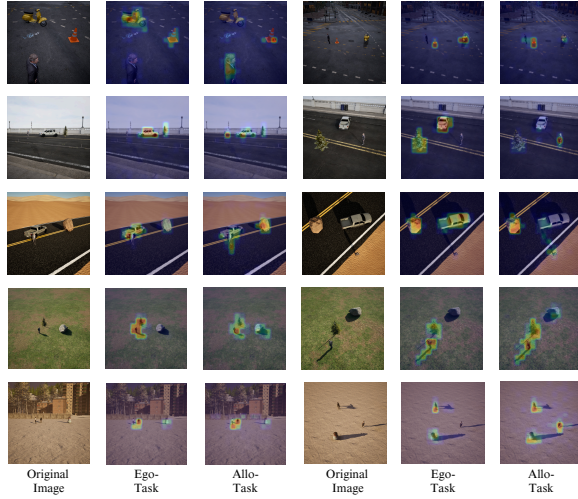


Fig. 17: Visualization of Task-Specific Attention Dynamics in Efficient Probing. We visualize the mean attention maps (averaged across 4 learned queries) extracted from an efficient probing head attached to a frozen VGGT backbone.

C Layer-wise Probing: Where is Spatial Information Encoded?

To understand how spatial reasoning emerges and evolves throughout the network depth, we evaluate the performance of intermediate layers as frozen features across both egocentric and allocentric tasks. For this analysis, we use VGGT and DINO-v2 (with register tokens), training an efficient probing head on the outputs of individual transformer blocks. To ensure that the observed trends reflect generalizable spatial skills rather than overfitting to specific visual domains, all reported results are averaged across the five diverse environments.

As illustrated in Figure 19, we observe a consistent trend across both model architectures and task types: spatial reasoning accuracy improves steadily through the initial layers, plateaus, and eventually peaks in the late-intermediate layers (specifically Layer 18 and 20 for a 24-layer ViT-L), rather than at the final output layer. This behavior aligns with findings from the Perception Encoder [81] and recent architectural analyses in DINOv3 [3]. In standard VFM, the final

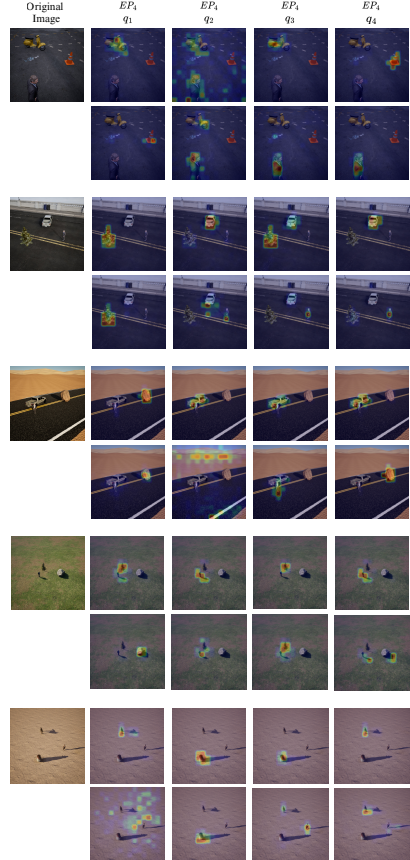


Fig. 18: Visualizing each head of multi-query attention. We visualize the attention maps of the four learnable queries from an efficient probing head attached to a frozen VGGT backbone. In each environment, the first image in the top row shows the original image. The first row shows the attention maps for the four queries ($q_1 \dots q_4$) solving the egocentric tasks, and the second row shows the attention maps for the allocentric tasks.

layers are often optimized for high-level semantic abstraction and invariance (e.g., classifying a "dog" regardless of its position). This objective implicitly encourages the model to discard precise geometric details in the final projection. Our results confirm that for tasks where geometry plays a governing role, such as the allocentric perspective-taking challenge, the most robust representations are located deeper in the network stack, before the last layer.

While the performance drop-off at the final layer is relatively minor, which makes it still a

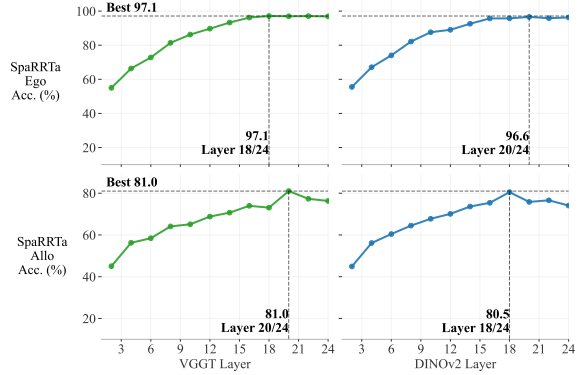


Fig. 19: Layer Analysis. We evaluate the spatial reasoning capability of intermediate features extracted from frozen VGGT and DINO-v2 (with registers) ViT Large backbones using efficient probing. Results are averaged across all five evaluation environments to ensure robustness against domain-specific bias. Vertical dashed lines denote the layer achieving peak performance.

viable default choice for general use, these results suggest that downstream embodied agents requiring precise spatial manipulation or reasoning can achieve optimal performance by tapping into these late-intermediate layers. Specifically, extracting features from Layer 18–20 for a ViT-Large yields a measurable improvement in accuracy, providing a free performance boost without additional training cost.